AD-A077 376 SRI INTERNATIONAL MENLO PARK CA F/G 19/1
LAGRANGE GAGE STUDIES OF NONIDEAL EXPLOSIVES CONTAINING NH SUB --ETC(U)
OCT 79 M COWPERTHWAITE , J T ROSENBERG DAAG29-76-C-0033
UNCLASSIFIED ARO-13925.1-CX NL

END
DATE FILMED
1 — 80
DDC

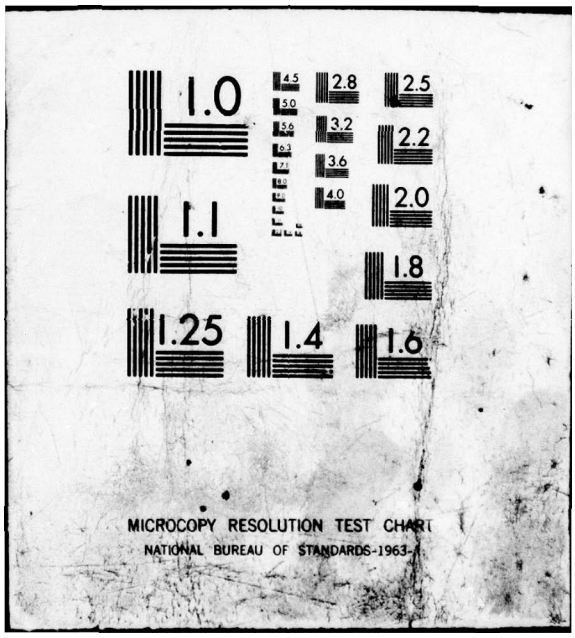
1.0
1.1
1.25
1.4
1.6
1.8
2.0
2.2
2.5
2.8
3.2
3.6
4.0
4.5
5.0
5.6
6.3
MICROCOPY RESOLUTION TEST CHART
NATIONAL BUREAU OF STANDARDS-1963-A

LAGRANGE GAGE STUDIES OF NONIDEAL EXPLOSIVES CONTAINING NH_4NO_3

Final Report

M. Cowperthwaite
J. T. Rosenberg

October 1979

U.S. ARMY RESEARCH OFFICE

Contract DAAG29-76-C-0033

SRI International
333 Ravenswood Avenue
Menlo Park, California 94025
(415) 326-6200
Cable: SRI INTL MPK
TWX: 910-373-1246

The view, opinions, and/or findings contained in this report are those of the author(s) and should not be construed as an official Department of the Army position, policy, or decision, unless so designated by other documentation.

UNCLASSIFIED

SECURITY CLASSIFICATION OF THIS PAGE (When Data Entered)

REPORT DOCUMENTATION PAGE

READ INSTRUCTIONS BEFORE COMPLETING FORM

1. REPORT NUMBER

2. GOVT ACCESSION NO.

3. RECIPIENT'S CATALOG NUMBER

4. TITLE (and Subtitle)

LAGRANGE GAGE STUDIES OF NONIDEAL EXPLOSIVES CONTAINING NH_4NO_3 NH sub 4 NO sub 3.

5. TYPE OF REPORT & PERIOD COVERED

Final 5-17-76 to 5-16-79

6. PERFORMING ORG. REPORT NUMBER

PYU-5414

7. AUTHOR(s)

M. Cowperthwaite
J. T. Rosenberg

8. CONTRACT OR GRANT NUMBER(s)

DAAG29-76-C-0033

9. PERFORMING ORGANIZATION NAME AND ADDRESS

SRI International
333 Ravenswood Avenue
Menlo Park, CA 94025

10. PROGRAM ELEMENT, PROJECT, TASK AREA & WORK UNIT NUMBERS

12 69

11. CONTROLLING OFFICE NAME AND ADDRESS

U.S. Army Research Office
P.O. Box 12211
Research Triangle Park, NC 27709

12. REPORT DATE

October 1979

13. NUMBER OF PAGES

68

14. MONITORING AGENCY NAME & ADDRESS (if different from Controlling Office)

Final rept. 17 May 76 - 16 May 79

15. SECURITY CLASS (of this report)

Unclassified

15a. DECLASSIFICATION/DOWNGRADING SCHEDULE

16. DISTRIBUTION STATEMENT (of this Report)

Approved for public release; distribution unlimited.

ARO 13925.1-CX

17. DISTRIBUTION STATEMENT (of the abstract entered in Block 20, if different from Report)

18. SUPPLEMENTARY NOTES

The view, opinions, and/or findings contained in this report are those of the authors and should not be construed as an official department of the Army position, policy, or decision unless so designated by other documentation.

19. KEY WORDS (Continue on reverse side if necessary and identify by block number)

Ideal detonation	Particle velocity gages	Reaction times
Nonideal detonation	Lagrange analysis	NH_4NO_3
Hugoniot curves	Amatex 20	
Chapman-Jouguet state	Composition B	
Embedded Lagrange gages	Detonation Parameters	

20. ABSTRACT (Continue on reverse side if necessary and identify by block number)

Theoretical and experimental studies of nonideal detonation in explosives containing constituents such as RDX and NH_4NO_3, which react at different rates, are presented in this report.

DD FORM 1 JAN 73 1473 EDITION OF 1 NOV 65 IS OBSOLETE

UNCLASSIFIED

SECURITY CLASSIFICATION OF THIS PAGE (When Data Entered)

H10 281

JAB

The theoretical study is based on the assumption that there is complete reaction of the faster reacting components but no reaction of the slower reacting component in the shock discontinuity at the front of the detonation wave. In this case, the fast and slow reactions are decoupled in the detonation process, and different types of flow are allowed by the equations of motion behind the reactive discontinuity. Such flows are categorized as (1) a nonreactive Taylor wave, (2) a steady-state reaction zone followed by a nonreactive Taylor wave, and (3) a nonsteady reaction zone followed by a nonreactive Taylor wave. These flows are discussed and solutions to the equations governing polytropic explosives are constructed to exemplify them.

The experimental study involved a multiple-Lagrange-gage investigation of the detonation processes in Amatex 20 and Composition B. Particle velocity histories were recorded at different Lagrange positions in both explosives. A new gage emplacement method was developed in which the bare 0.15-mm-thick aluminum gages were embedded in the targets during casting. This technique eliminates the necessity to machine the study materials and minimizes perturbations to the flows being measured. These measured particle velocity histories were used in the Lagrange analysis to determine the sequence of states attained in the detonation waves. The calculated loading and unloading paths in the pressure--particle-velocity and pressure--specific-volume planes show that the detonation processes are self-sustaining in Amatex 20 and Composition B. The states calculated in the Lagrange analysis were used with the Chapman-Jouguet (CJ) condition to determine CJ parameters and to resolve the reaction zones in these explosives. The following determinations were made.

Parameter	Amatex 20	Composition B
Detonation velocity	6.95 mm/μsec	7.86 mm/μsec
Reaction time	0.3 μsec	0.1 μsec
Pressure	225 kbar	295 kbar
Particle velocity	2.01 mm/μsec	2.19 mm/μsec
Specific volume	0.441 cm^3/g	0.420 cm^3/g
Polytropic index at CJ point	2.46	2.58

The difference in reaction times is taken as evidence that the ammonium nitrate reacts to support the propagation of the detonation wave in Amatex 20. If the reaction of the ammonium nitrate is complete at the CJ point, the detonation process in Amatex 20 is ideal in the sense that the detonation process in Composition B is ideal. Thermodynamic calculations, using a code such as the TIGER code, are required to determine the amount of ammonium nitrate that has reacted at the CJ point.

CONTENTS

LIST OF ILLUSTRATIONS

LIST OF TABLES

1. INTRODUCTION

We first introduce the terms "ideal" and "nonideal" detonations used in this report. Detonations will be called ideal when they can be modeled satisfactorily with the one-dimensional Chapman-Jouguet (CJ) model of detonation, and nonideal when they cannot. An explicit assumption in this CJ model is that all the explosive reacts in the detonation process. Similarly, explosives will be called ideal when they exhibit ideal detonation, and nonideal when they do not. The present research is concerned with the nonideal detonation process that occurs in composite explosives containing ammonium nitrate (NH_4NO_3). The object of the work is to understand the nonideal detonation process in these explosives and to formulate a satisfactory model for calculating their detonation parameters.

Theoretical and experimental studies were undertaken in our approach to this problem. In the theoretical study, nonideal detonation was treated as shock-induced hydrodynamic flow with a fast-reacting component liberating energy in a shock discontinuity at the wave front and a slowly reacting component liberating energy behind the wave front. In the experimental study, Lagrange particle velocity gages were used to characterize detonation by determining the sequence of states attained during compression and rarefaction in the detonation process.

The explosive materials chosen for this experimental program are Amatex 20 and Composition B. We consider these materials as belonging to a class of composite explosives containing TNT, RDX, and NH_4NO_3. By weight, Amatex 20 contains 40% TNT, 20% RDX, and 40% NH_4NO_3; Composition B contains 36% TNT and 64% RDX. Amatex 20 was selected as a documented and easily fabricated military explosive containing a large percentage of NH_4NO_3, and Composition B was chosen as the baseline ideal explosive for the study. Basic differences among the particle velocity histories recorded in detonating Amatex 20 and Composition B were expected to provide an understanding of the role of NH_4NO_3 in the detonation process.

2. THEORETICAL STUDY

In the theoretical study, attention was given to the problem of extending the CJ model for ideal detonation to a satisfactory model for nonideal detonation. For practical purposes, a self-sustaining detonation in an ideal explosive such as RDX can be modeled as a reactive CJ discontinuity followed by an nonreactive Taylor wave. The chemical energy supporting the detonation is liberated in the shock at the front of the wave, and the subsequent adiabatic expansion of the detonation products is governed by the rear-boundary conditions. A more complicated treatment of self-sustaining detonation is needed for nonideal explosives, such as Amatex compositions, because their different explosive constituents react at different rates.

Let us now introduce the notation used to describe the one dimensional flows. Time is donated by t, Lagrange distance by h, specific volume by v, particle velocity by u, pressure by p, and specific energy by e; the subscript o denotes the constant state ahead of the wave. The shock discontinuity at the wave front is governed by the Rankine-Hugoniot jump conditions,

$$v_H D = v_o(D - u_H) \ , \tag{1}$$

$$p_H = (D/v_o)^2 \ (v_H - v_o) = Du_H/v_o, \tag{2}$$

and

$$e_H - e_o = \frac{1}{2} \ p_H(v_o - v_H) \ , \tag{3}$$

where D denotes the shock velocity and the subscript H denotes the shocked condition at the wave front. The adiabatic invisid flow in the wave behind the shock is governed by the following expressions of the laws of conservation of mass, momentum, and energy:

$$\frac{\partial v}{\partial t} = v_o \frac{\partial u}{\partial h} \quad , \tag{4}$$

$$\frac{\partial u}{\partial t} = - v_o \frac{\partial p}{\partial h} \quad , \tag{5}$$

and

$$\frac{\partial e}{\partial t} = - p \frac{\partial v}{\partial t} \quad . \tag{6}$$

The flow and chemistry are coupled by the dependence of e on the reaction coordinates. Let the subscripts 1 and 2 denote the faster and slower reacting components, α_1 and α_2 their respective mass fractions, λ_1 and λ_2 their respective reaction coordinates, and let the superscript o denote the standard state. The reaction coordinates are defined to lie between 0 and 1 so that $\lambda_1 = \lambda_2 = 0$ denotes no reaction, and $\lambda_1 = \lambda_2 = 1$ denotes complete reaction. Neglecting the initial pressure, we can write the initial internal energy of the composite explosive as $e_o = \alpha_1 \Delta h_1^o + \alpha_2 \Delta h_2^o$, where Δh_1^o and Δh_2^o denote the specific heats of formation of the faster and slower reacting components. We can also write the internal energy of the explosive mixture as

$$e = \alpha_1 \Delta h_1^o + \alpha_2 \Delta h_2^o - \lambda_1 \alpha_1 Q_1 - \lambda_2 \alpha_2 Q_2 + \tilde{e}(p, v, \lambda_1, \lambda_2), \tag{7}$$

where Q_1 and Q_2 denote the heats of reaction of the faster and the slower reacting components.

At this stage it is convenient to introduce the polytropic equation of state for the explosive mixture. We use the polytropic equation of state in the theoretical studies in this report because it accounts for essential features of the explosive mixture and simplifies the Hugoniot curve calculations. With the assumption that the polytropic index has the same value for each explosive constituent and is a constant k, Eq. (7) can be written as

$$e = e_o - \lambda_1 q_1 - \lambda_2 q_2 + \frac{pv}{k-1} \quad , \tag{8}$$

with $q_1 = \alpha_1 Q_1$ and $q_2 = \alpha_2 Q_2$.

Our treatment of detonation is based on the assumption that wave propagation in ideal detonation is supported by all the chemical energy and that in nonideal detonation it is not so supported. States attained in ideal detonation by our two component mixture thus satisfy the condition $\lambda_1 = \lambda_2 = 1$. To treat the states attained in nonideal detonation we assume that the faster reacting component, such as RDX or TNT, reacts in the shock at the wave front, but that the slower reacting component, such as NH_4NO_3, does not. In this case, $\lambda_1 = 1$ and $\lambda_2 = 0$ at the shock front, Eq. (7) for material behind the shock can be written as

$$e = e_o - q_1 - \lambda_2 q_2 + \tilde{e}(p,v,\lambda_2), \tag{9}$$

and the corresponding equation for polytropic material is obtained by setting $\lambda_1 = 1$ in Eq. (8). The equations $\lambda_2 = \partial\lambda_2/\partial t = 0$ express the condition that the slower reacting component does not react behind the shock front. When $\partial\lambda_2/\partial t \neq 0$ behind the shock, the combination of Eqs. (6) and (9) gives the equation

$$\frac{\partial p}{\partial t} = -\left(\frac{c}{v}\right)^2 \frac{\partial v}{\partial t} + \frac{\Gamma}{v}\left[q_2 - \left(\frac{\partial \tilde{e}}{\partial \lambda_2}\right)\right]\frac{\partial \lambda_2}{\partial t}, \tag{10}$$

where the sound speed c satisfies the identity

$$\left(\frac{c}{v}\right)^2 - = \frac{p + (\partial e/\partial v)}{(\partial e/\partial p)}, \tag{11}$$

and the Grüneisen parameter $\Gamma/v = (\partial e/\partial p)$. For polytropic material, c and Γ are related to k by the equations $c^2 = kpv$ and $\Gamma = k - 1$, respectively, and $(\partial\tilde{e}/\partial\lambda_2) = 0$.

We will now use the polytropic equation of state to define states attained at the wave front in our treatment of detonation. These shocked states lie on the Hugoniot curve defined by the Hugoniot equation (3) and the polytropic relationship, Eq. (8). The combination of Eqs. (3) and (8) with the condition $\lambda_1 = 1$ gives the equation for the Hugoniot curves of polytropic explosive as

$$p_H = \frac{2(q_1 + \lambda_2 q_2)}{\mu v_H - v_o} \quad , \tag{12}$$

where $\mu = (k+1)/(k-1)$.

Equation (12) defines a family of Hugoniot curves in the (p,v) plane with the reaction coordinate λ_2 the parameter of the family. The Hugoniot curve with $\lambda_2 = 0$ defines the locus of shocked states connected to the initial state when the reaction of the faster component is complete in the shock discontinuity. The Hugoniot with $\lambda_2 = 1$ defines the locus of shocked states connected to the initial state in the ideal detonation process when the reactions of both the faster and slower components are complete in the shock discontinuity. In this case, the detonation parameters of the unsupported ideal detonation wave are defined by the CJ condition $D = u + c$. At the CJ point, the entropy is a minimum on the Hugoniot curve, and the Hugoniot curve and the isentrope are tangent to the Rayleigh line defined by Eq. (2).

The combination of Eqs. (1) and (2) with the CJ condition and the equation for the sound speed gives the following equations for the CJ volume, CJ sound speed, and CJ particle velocity:

$$v_{CJ} = \frac{k}{k+1} v_o \quad , \tag{13}$$

$$c_{CJ} = \frac{k}{k+1} D \quad , \tag{14}$$

and

$$u_{CJ} = \frac{D}{k+1} \quad . \tag{15}$$

The equation for the detonation velocity then follows by combining Eqs. (1), (2), and (12) as

$$D^2 = 2(k^2 - 1)\ (q_1 + q_2) \quad , \tag{16}$$

and the equation for nonideal detonation with $\lambda_2 = 0$ as

$$D^2 = 2(k^2 - 1)q_1 \quad . \tag{17}$$

To simplify the calculation of the Hugoniot curves, we assume that the heats of reaction of the faster and slower reacting components are equal, set $Q_1 = Q_2 = Q$ accordingly, and set $\alpha_1 = 1$, $\alpha_2 = 0$, and $\lambda_1 = \lambda'$. As a result, states attained at the wave front in nonideal detonation lie on the partially-reacted Hugoniot curves of the faster reacting component. The combination of Eq. (3) and the polytropic relationship gives the equation for these Hugoniot curves as

$$P_H = \frac{\rho_o D^2}{(k^2-1)(\mu V-1)} , \tag{18}$$

where $V = v_H/v_o$, and the equation for the CJ velocities as

$$D^2 = 2(k^2-1)\lambda' Q . \tag{19}$$

Plots of Eq. (18) with $\rho_o = 1.6$ cm^3/g, D = 7 mm/μsec, and k = 3 are shown in Figure 1. The fully-reacted Hugoniot curve with $\lambda' = 1$ is shown as ECH and the partially-reacted Hugoniot with $\lambda' = 0.8$ as E′C′H′. The constant volume explosion points are shown as E and E′, and the Rayleigh lines, defining the CJ points at C and C′, are shown as OCR and OC′R′.

Under the assumption that there is complete reaction of the faster component but no reaction of the slower component in the shock discontinuity, the fast and slow reactions are decoupled in the nonideal detonation wave. In this case, different types of flow behind the reactive discontinuity are allowed by the equations of motion, Eqs. (4), (5), and (10). Such flows are categorized here as (1) a nonreactive Taylor wave, (2) a steady-state reaction zone followed by a nonreactive Taylor wave, and (3) a nonsteady reaction zone followed by a nonreactive Taylor wave. These flows will now be discussed in more detail; when convenient, the polytropic equation of state will be used to exemplify them.

A Nonreactive Taylor Wave

In the case of the nonreactive Taylor wave, the slower reacting component does not react behind the shock, $\lambda_2 = 0$, and the detonation is equivalent to an ideal detonation with a reduced heat of reaction $q_1 = \alpha_1 Q_1$.

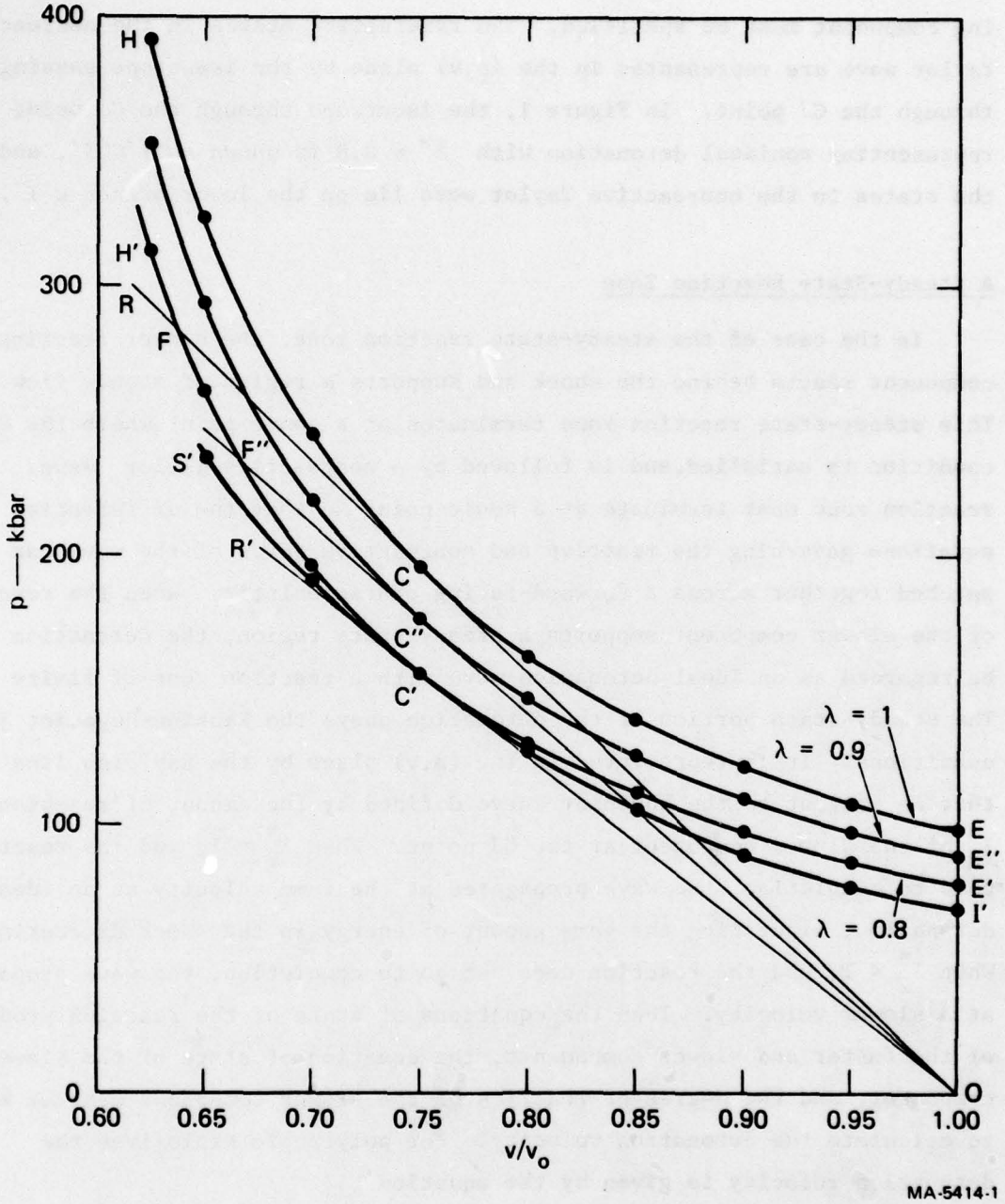

FIGURE 1 REACTIVE HUGONIOT CURVES FOR POLYTROPIC EXPLOSIVE

To calculate the Hugoniot curve of the explosive mixture and the detonation parameters, using a code such as the TIGER code,[1] the equations of state of the reaction products of the faster reacting component and of the nonreacting component must be specified. The rarefactive states in the nonreactive Taylor wave are represented in the (p,v) plane by the isentrope passing through the CJ point. In Figure 1, the isentrope through the CJ point representing nonideal detonation with $\lambda' = 0.8$ is shown as I'C'S', and the states in the nonreactive Taylor wave lie on the lower branch C'I'.

A Steady-State Reaction Zone

In the case of the steady-state reaction zone, the slower reacting component reacts behind the shock and supports a region of steady flow. This steady-state reaction zone terminates at a sonic point,where the CJ condition is satisfied,and is followed by a nonreactive Taylor wave. The reaction zone must terminate at a sonic point so that the differential equations governing the reactive and nonreactive parts of the wave can be patched together across a forward-facing characteristic. When the reaction of the slower component supports a steady-state region, the detonation can be regarded as an ideal detonation wave with a reaction zone of finite width. The steady-state portion of the detonation obeys the Rankine-Hugoniot jump conditions. It is represented in the (p,v) plane by the Rayleigh line that is tangent to the Hugoniot curve defined by the amount of reaction λ_2^* of the slower component at the CJ point. When $\lambda_2^* = 1$, and the reaction goes to completion, the wave propagates at the same velocity as an ideal detonation, liberating the same amount of energy in the shock discontinuity. When $\lambda_2^* < 1$, and the reaction does not go to completion, the wave propagates at a slower velocity. Then the equations of state of the reaction products of the faster and slower components, the equation of state of the slower component, and the degree of reaction of the slower component must be known to calculate the detonation velocity. For polytropic explosives the detonation velocity is given by the equation

$$D = \left(2(k^2 - 1)(q_1 + \lambda_2^* q_2)\right)^{1/2} ;$$

it increases from $D = \left[2(k^2 - 1)q_1\right]^{1/2}$ to $D = \left[2(k^2 - 1)(q_1 + q_2)\right]^{1/2}$ as the reaction coordinate λ_2^* at the CJ point increases from 0 to 1. The differential equation relating u and λ_2 in the steady-state portion of the wave is obtained readily as

$$\left[(D - u) - ku\right] \frac{\partial u}{\partial t} = (k - 1)q_2 \frac{\partial \lambda_2}{\partial t} \quad , \tag{20}$$

by combining the energy equation derived from Eq. (10),

$$\frac{\partial p}{\partial t} = - \frac{kp}{v} \frac{\partial v}{\partial t} + \frac{(k-1)}{v} q_2 \frac{\partial \lambda_2}{\partial t} \tag{21}$$

with the relationship between $\partial p/\partial t$ and $\partial u/\partial t$ and the relationship between $\partial v/\partial t$ and $\partial u/\partial t$ obtained by differentiating the jump conditions in Eqs. (2). Integrating Eq. (20) and setting $\lambda_2 = \lambda_2^*$ at the CJ point where (D-u) = ku, gives the relationship between u and λ_2 in the steady-state portion of the wave as

$$u = \frac{D}{k+1} + \frac{\left[2(k^2-1)q_2(\lambda_2^* - \lambda_2)\right]^{1/2}}{(k+1)} \quad , \tag{22}$$

where $D = \left[2(k^2 - 1)(q_1 + \lambda_2^* q_2)\right]^{1/2}$. Setting $\lambda_2 = 0$ and rearranging Eq. (22) gives the equation for the particle velocity at the wave front as

$$\frac{u_H}{D} = \frac{1}{(k+1)} + \frac{1}{(k+1)} \left[\frac{\lambda_2^* q_2}{q_1 + \lambda_2^* q_2}\right]^{1/2} . \tag{23}$$

Combining Eq. (21) with the relationship between $\partial p/\partial t$ and $\partial v/\partial t$ obtained by differentiating Eq. (2) gives the differential equation relating v and λ_2 in the steady-state portion of the wave as

$$\left[k\, v_o - (k + 1)v\right] \frac{\partial v}{\partial t} = (k - 1)\left[\frac{v_o}{D}\right]^2 q_2 \frac{\partial \lambda_2}{\partial t} \quad . \tag{24}$$

Integrating Eq. (24) and setting $\lambda_2 = \lambda_2^*$ at the CJ point where $k\, v_o - (k + 1)v = 0$ gives the relationship between v and λ_2 in the steady-state portion of the wave as

$$\left[k\, v_o - (k + 1)v\right]^2 = \left[\frac{v_o^2\, q_2}{q_1 + \lambda_2^* q_2}\right](\lambda_2^* - \lambda_2) \quad . \tag{25}$$

The equation for the volume at the wave front is then obtained by setting $\lambda_2 = 0$ in Eq. (25) as

$$\frac{v_H}{v_o} = \frac{k}{k+1} - \frac{1}{(k+1)}\left[\frac{\lambda_2^* q_2}{q_1 + \lambda_2^* q_2}\right]^{1/2} \quad . \tag{26}$$

In Figure 1, the family of steady-state waves is represented by the family of Rayleigh lines lying between $OC'R'$ and OCR. Since $Q_1 = Q_2 = Q$, $\alpha_1 = \lambda'$ $\alpha_2 = (1 - \lambda')$, and $\lambda_2 = (\lambda - \lambda')/(1 - \lambda')$ in this case, the volume at the wave front is given by the equation

$$\frac{v_H}{v_o} = \frac{k}{k+1} - \frac{1}{(k+1)}\left[1 - \frac{\lambda'}{\lambda^*}\right]^{1/2} \tag{27}$$

where λ^* denotes the reaction coordinate at the CJ point. The point representing the wave front in Figure 1 moves along the partially-reacted Hugoniot curve $E'C'H'$ from C' to F as the value of λ^* increases from $\lambda' = 0.8$ to 1. When $\lambda^* = 0.9$, the reactive shock discontinuity at the wave front is represented by the Rayleigh line OF'', and the steady-state portion of the wave is represented by F'' C''. States in the nonreactive Taylor wave following this steady-state flow are represented by points on the isentrope passing through C'' with $V \geq 0.75$; however, this isentrope is not shown in Figure 1.

A Nonsteady Reaction Zone

In the case of the nonsteady reaction zone, the slower reacting component reacts behind the shock and supports a region of nonsteady flow. The flow can be considered as a reactive Taylor wave. As was true of the

steady-state flow, however, the reaction must terminate at a sonic point so that the reactive Taylor wave and the ensuing nonreactive Taylor wave can be patched together across a forward-facing characteristic. When the propagation velocity of the wave is constant, it follows from previous work[2] that the solution for such a flow in a polytropic explosive can be written in terms of the similarity parameter

$$\xi = \frac{t/\alpha + 1}{h/\beta + 1} \quad , \tag{28}$$

as

$$v = v_H \, V(\xi) \quad , \tag{29}$$

$$u = u_H \, U(\xi) \quad , \tag{30}$$

$$p = p_H \, P(\xi) \quad , \tag{31}$$

and

$$\lambda_2 = \Lambda(\xi), \tag{32}$$

where α is a characteristic time and β is a characteristic distance. The similarity parameter ξ is equal to 1 along the shock path, and it follows from Eq. (28) that β and α are related to the propagation velocity by the equation $\beta = D\alpha$. The functions $V(\xi)$, $U(\xi)$, $P(\xi)$ and $\Lambda(\xi)$ are related by the equations of motion and satisfy the conditions $V(1) = U(1) = P(1) = 1$ and $\Lambda(1) = 0$ at the shock front. The ordinary differential equations relating these functions are obtained as

$$\frac{dV}{d\xi} = - A\xi \frac{dU}{d\xi} \quad , \tag{33}$$

$$\frac{dU}{d\xi} = \xi \frac{dP}{d\xi} \quad , \tag{34}$$

and

$$(V - kA\xi^2 P)\frac{dP}{d\xi} = (k - 1)\left[\frac{q_2}{p_H u_H}\right]\frac{d\Lambda}{d\xi} \quad . \tag{35}$$

where $A = (v_o u_H / v_H D)$, by substituting the partial derivatives of the flow variables calculated from Eqs. (28) - (32) into Eqs. (4), (5), and (21).

Flow conditions at the wave front are defined by Eqs. (33-35). We first consider the energy equation Eq. (35). It follows from Eq. (1) that at the wave front

$$(V - kA\xi^2 P)_H = (k + 1) - k\left[\frac{v_o}{v_H}\right], \tag{36}$$

because $V(1) = P(1) = \xi_H = 1$. We also assume that states on the Hugoniot curve, defined by $\lambda_1 = 1$, and $\lambda_2 = 0$, that lie below the CJ point do not represent shocked states at the wave front. In this case, when $d\Lambda/d\xi_H > 0$ and $v_H < k\, v_o/(k+1)$, it follows from Eq. (35) that $dP/d\xi_H < 0$; it then follows from Eqs. (34) and (33) that $dU/d\xi_{H_2} < 0$ and $dV/d\xi_H > 0$. Moreover, $d\Lambda/d\xi = 0$ at the CJ point where $(V - kA\xi^2 P)_H = 0$. It follows from these conditions that when the state at the wave front lies above C´ on the frozen Hugoniot E´C´H´(Figure 1), the reaction of the slower component causes the pressure and particle velocity to decrease at the wave front but the volume to increase.

We now consider conditions for patching the equations governing the reactive Taylor wave to those governing the nonreactive Taylor wave. The equations can be patched together across a similarity line for the reactive flow when the similarity line is also a forward-facing C_+ characteristic. The condition for patching the equations is thus that the C_+ characteristic is a straight line. The C_+ characteristics are governed by the equations

$$\frac{dh}{dt} = \frac{v_o c}{v} = v_o\left[\frac{kp_H}{v_H}\right]^{1/2} C(\eta)\ , \tag{37}$$

where $C(\eta) = (P(\eta)/V(\eta))^{1/2}$. Combining the equations obtained by differentiating Eqs. (37) and (28) leads to the equation

$$(h/\beta + 1)\,\frac{d^2h}{dt^2} = \frac{v_o}{\alpha}\left[\frac{k\ p_H}{v_H}\right]^{1/2} \frac{dC}{d\eta}\left[1 - \frac{\xi}{D}\frac{dh}{dt}\right], \tag{38}$$

which shows that a C_+ characteristic will be a straight line when it satisfied the conditions

$$\frac{dh}{dt} = \frac{D}{\xi} = v_o\left[\frac{k\ p_H}{v_H}\right]^{1/2} C(\eta)\ . \tag{39}$$

Squaring the terms in Eq. (39) and eliminating D^2 by using the jump conditions, shows that the C_+ characteristic will be a straight line and the condition will be satisfied when

$$(V - kA\xi^2 P) = 0. \tag{40}$$

It follows from Eq. (35) that the reaction rate must be zero, $d\Lambda/d\xi = 0$, along the C_+ characteristic where the reactive and nonreactive Taylor waves are patched together.

3. EXPERIMENTS

Six experiments were performed to measure multiple Lagrange* particle velocity histories within the two study materials, Amatex 20 and Composition B, while they undergo self-sustaining planar detonation. A new method was developed for embedding particle velocity gages within the targets. The method, which requires no interior machined cuts or glue lines, is a significant advancement in Lagrange gage technology for high explosives (HE), because it minimizes the perturbing effects of the measurements on the flow and on the chemical reaction. Successful experiments were performed in each study material. In the following sections we describe the experimental procedures and present the resulting data.

General Experimental Configuration

The basic configuration used in all experiments is shown in Figure 2. A 20-cm-diameter plane-wave HE lens (P-80) initiated an HE driver system that in turn provided a planar shock input pulse to the Amatex or Composition B target. Particle velocity histories at various Lagrange positions in the target were measured with embedded electromagnetic particle velocity (EPV) gages. Expendable Helmholtz coils on plywood frames provided a uniform magnetic field for the EPV gages.

EPV Gages and Instrumentation

Studies involving the use of a single EPV gage within, or on the back surface of, a reacting charge have been presented by several authors.[3-8] Recently, Cowperthwaite and Rosenberg described the use of multiple EPV gages within single charges of initiating cast and pressed TNT.[9] In the present work, multiple EPV gages are used within detonating, single charges of Amatex 20 and Composition B.

---

*The term Lagrange refers to an observation made at a specific material element in the flow; the term Eulerian refers to an observation made at a specific position fixed in the laboratory reference frame.

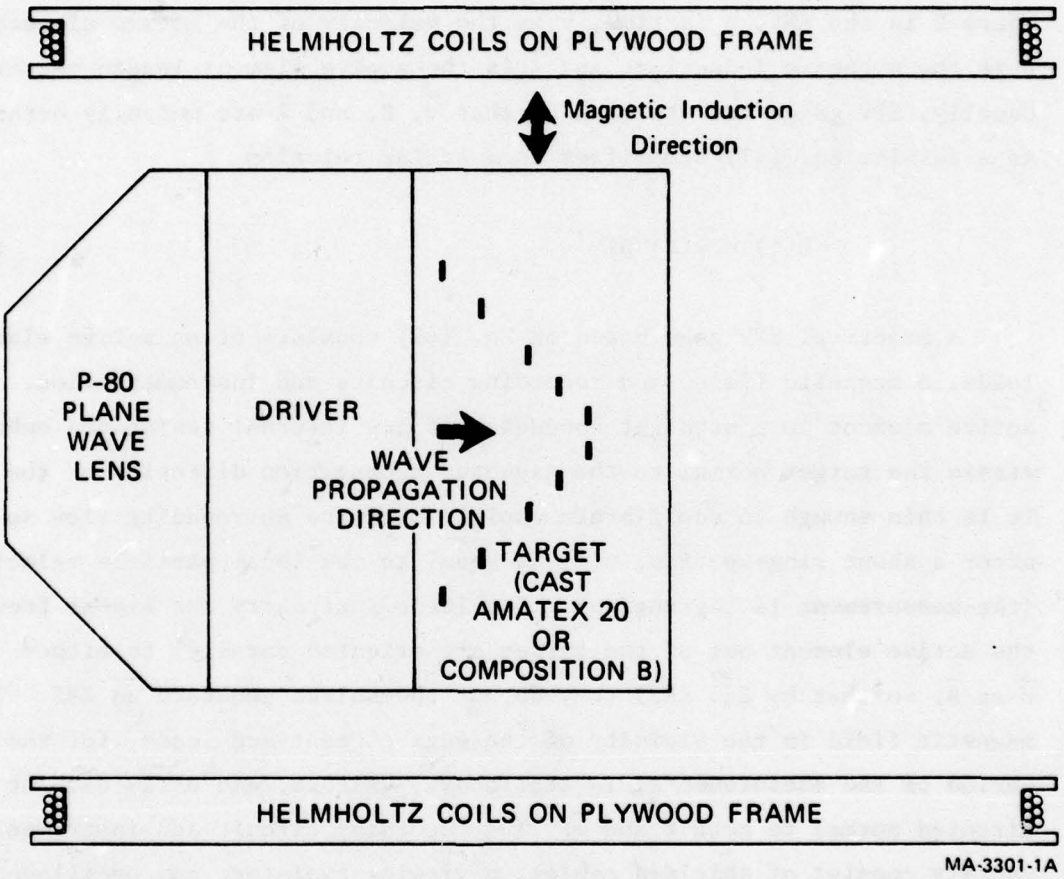

FIGURE 2 CONFIGURATION OF EMBEDDED PARTICLE VELOCITY GAGE EXPERIMENTS (NOT TO SCALE)

The vertical lines in the target represent cross sections of the active elements of individual electromagnetic particle velocity gages; ten gages are indicated.

The principle of the EPV gage is that an electrical conductor moving in a fixed magnetic field will experience a motional electromotive force (EMF) proportional to its velocity. By Faraday's law of induction for moving circuits[10] the EMF may be expressed as

$$E(t) = (\vec{v}(t) \times \vec{B}) \cdot \vec{\ell} \tag{41}$$

where E is the EMF, t is time, $\vec{v}$ is the velocity of the active element, $\vec{B}$ is the magnetic induction, and $\vec{\ell}$ is the active element length vector. Usually, EPV gages are designed so that $\vec{v}$, $\vec{B}$, and $\vec{\ell}$ are mutually orthogonal. As a result, Eq. (41) simplifies to a scalar relation

$$E(t) = v(t)\, B\ell \tag{42}$$

A practical EPV gage based on Eq. (42) consists of an active element, leads, a magnetic field, and recording circuits and instrumentation. The active element is a straight conductor of low internal resistance embedded within the target normal to the expected propagation direction of the wave. It is thin enough to equilibrate rapidly with the surrounding flow so that after a short ring-up time, v(t) is equal to the local particle velocity (the measurement is Lagrangian). The leads that carry the signal from the active element out of the target are oriented parallel to either $\vec{v}$ or $\vec{B}$, so that by Eq. (41) they do not themselves generate an EMF. The magnetic field in the vicinity of the gage element and leads, for the period of the measurements, is stationary, uniform, and uniaxial. It is directed normal to both $\vec{\ell}$ and $\vec{v}$. The recording circuit and instrumentation usually consist of shielded cables, a viewing resistor, and oscilloscopes to observe the potential drop across the viewing resistor. Techniques suitable for recording 100 MHz frequencies are employed, and corrections for obtaining the EMF from the recorded potential difference are applied if necessary. The specific EPV gage components used in this program are described below.

Active Element

Gage elements were aluminum foil strips 2.54 mm wide by 25.5 mm long by 0.127 mm thick for the Amatex 20 experiments; the strips used in the Co,position B experiments had the same dimensions except that they were 0.165 mm thick. Aluminum was used because it is a better impedance match to HE reaction products than other convenient good conductors, because it is chemically compatible with the study materials, and because it has sufficient mechanical stiffness for the gage emplacement process (described in the next section). The relatively large gage thicknesses were chosen both for mechanical strength (see next section) and because Edwards et al.[6] demonstrated that in detonating TNT, aluminum gages thinner than 0.127 mm are partially shunted electrically by the conductive reaction products.

Leads

Leads were formed from the same aluminum strips as the active elements by bending the strips in a specially constructed jig. The leads were aligned parallel to the wave propagation direction, that is, parallel to $\vec{v}$, and exited from the rear of the target. Additional information, including a photograph showing the gage geometry, is given in the target section.

Magnetic Field

The stationery uniaxial magnetic field at the gage elements was generated by expendable Helmholz coils of No. 8 Formvar-insulated copper wire wound on plywood frames. The coils contained 40 or 44 turns each with a mean radius of 40.6 cm. They were driven by a capacitor discharge system of about 400 μF operated at about 2 kV. This system results in a current of about 500 A in the coils and a magnetic induction of 450 G in the test region. The coil-capacitor discharge system has a time constant of about 2 msec, so the current and magnetic field are constant to within much better than 1% during the test time of about [illegible] sec. In each experiment, the current was measured by an inductive coil method and the magnetic induction $\vec{B}$ was calculated from the analytical expression for the response of Helmholtz coils.

Recording Circuits and Instrumentation

Each gage drove a pair of either RG-213 or RG-58 (depending on length) coaxial cables with grounded shields resistively terminated in their characteristic 51-Ω impedances. The voltage drops across each pair of terminating resistors were recorded differentially with Tektronix oscilloscopes and amplifiers having rise times of 2-12 nsec. Differential recording was used to reduce susceptibility to common-mode noise pickup and to shifts in ground potential. Because of the low impedance of the active elements in the gages, relative to the 51-Ω terminating-viewing resistors, the recorded potential differences are equal to the gage EMFs to well within 1%.

Usually, two oscilloscopes monitored each gage. Sweep-speeds were 0.5, 1, or 2 μsec/cm, and vertical sensitivities were 100-200 mV/cm. After each shot sequence, sweep-speed and dc voltage sensitivity calibrations were performed at several spots on the face of each oscilloscope. Oscilloscope records were correlated in time by using a high-frequency repetitive pulse generator, operating typically at 0.5 MHz, to blank the beams (Z-axis modulation) of the Tektronix oscilloscopes. This system produces a sequence of essentially* simultaneous fiducial blanks on each of the oscillographs from one experiment.

Targets

A new technique for emplacing multiple Lagrange EPV gages within HE targets was developed and used in this program. With this technique, which is applicable to castable HE compositions, the gages are embedded within the target while it is being cast. Formerly targets were constructed by (1) wrapping the gages around tightly-fitting block of target material that were accurately machined to the shapes necessitated by gage and target requirements and grooved to accommodate the gages, (2) assembling the blocks, and (3) gluing them together, taking care to fill any voids. Development of the new technique was necessary because

*Corrections for differences in cable lengths are made but are essentially negligible at these relatively slow sweep speeds.

we were advised by J. Hershkowitz of the US Army Armament Research and Development Command (ARDAR-LCA), Dover, New Jersey, that it was not feasible to machine Amatex 20 to the complex shapes and close tolerances required by the earlier approach. The new method, which requires that the gages retain their shape through the HE pouring and solidification step, complicates the precise determination of the final relative positions of the gages within the target. Nonetheless, it is a major advancement in the study of explosives by internal Lagrange gages because it minimizes gage perturbations to the flow and the chemistry and it optimizes coupling of the gages to the surrounding motion.

Construction of targets with cast-in-place gages required the following steps: gage-block construction and testing, target casting, gage location determination, and characterization of the as-cast study material. These steps are described below.

Gage-Block Assembly

Linen-phenolic (Micarta*) gage locks were used to hold the gages during casting. A completed gage block assembly is shown in Figure 3. A bending jig was used to preform the aluminum strips for the EPV gages into piecewise linear U-shapes (see Figure 3) with active elements (cross bars of the U) uniformly 25.5 mm long and active elements and leads as nearly straight and perpendicular as possible. The gages were then precisely positioned horizontally and vertically with respect to each other with an accurately machined and measured step-jig. With the step-jig in place, the gages were bonded into grooves in the side of the Micarta gage block and the jig was removed. On the basis of photographic measurements and mechanical comparisons with the jig, gage separations in the completed blocks were estimated to coincide with step heights in the jig to within 0.05 mm. The leads were wrapped slightly less than half way around the back of the blocks (not shown in Figure 3) where miniature machine screws were used to hold down the leads and later, at the site, to connect instrumentation cables to the gages.

*Registered trade mark of Westinghouse Electric Company.

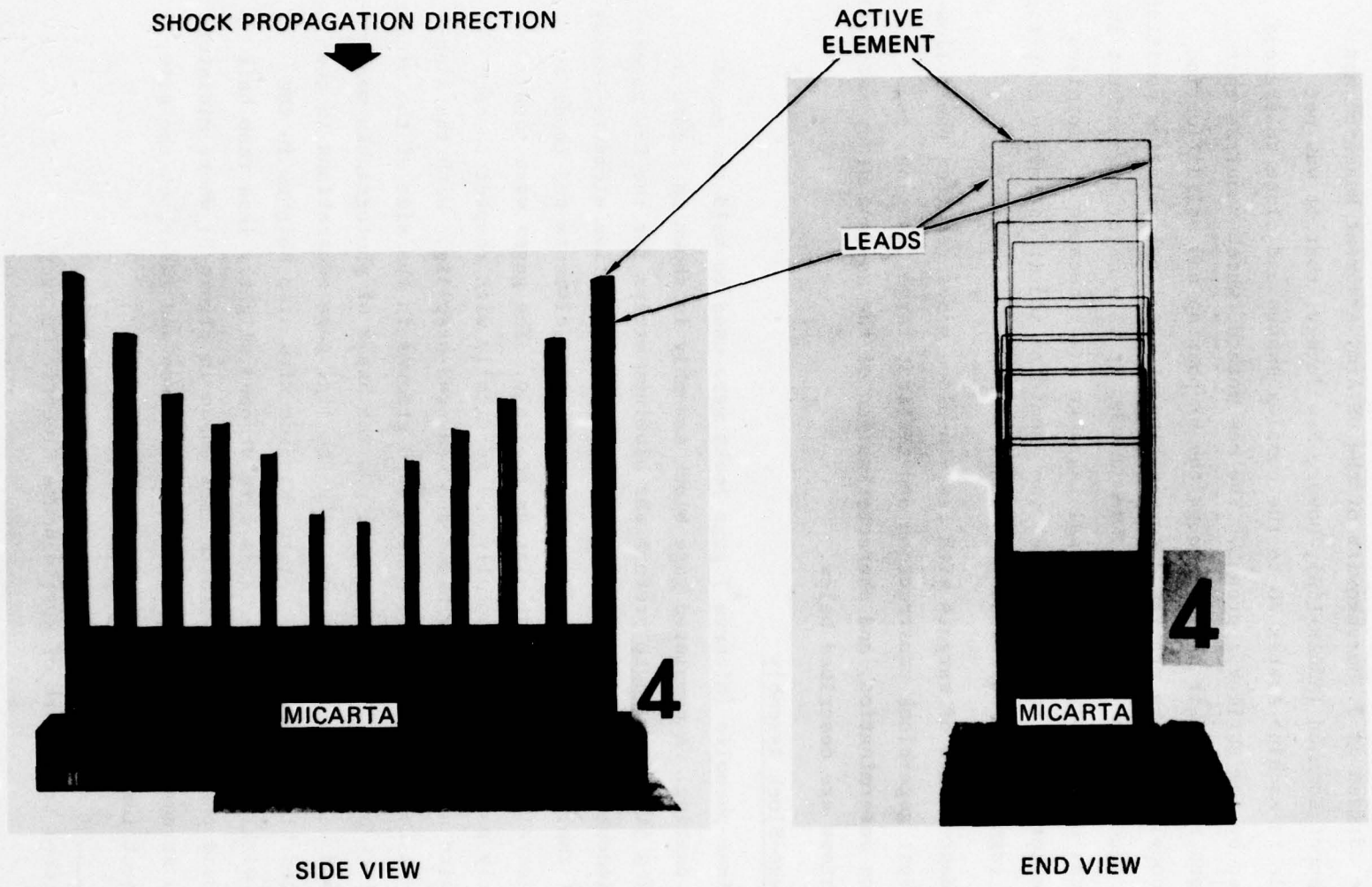

FIGURE 3 GAGE-BLOCK ASSEMBLY NUMBER 4

Independent aluminum gages (12 in this case) are mounted on a Micarta block producing a gage-block assembly ready for casting into the HE target. The active element and leads of one gage are indicated.

The individual gages must hold their shapes and dimensions while the completed gage blocks are handled, shipped, and cast into the HE targets. When attached to the gage blocks, the gages were quite rigid. On the basis of simple shake tests, we judged that they were sufficiently strong if handled and slipped in protective packages. To investigate gage stability during casting, we cast a prototype gage block in an explosive simulant. The simulant, termed Type II Filler-Simulant, was suggested by J. Hershkowitz, Arradcom. It was mixed to the efflux viscosity range of molten Amatex 20, a casting was made, and the completed casting was sectioned and examined in the vicinity of the gages. No gage distortions, displacements, or other casting problems were detected.

The gage blocks for the Amatex 20 and Composition B experiments were designed and constructed at SRI and shipped to Los Alamos Scientific Laboratories (LASL) for HE casting. The Amatex 20 gage blocks had 12 gages, two sets of six each arranged as shown in Figure 3; the Composition B blocks had 10, two sets of five each, also arranged in the pattern shown in Figure 3 (tallest frontside and shortest in center). The lateral center-to-center spacing between gages was 10 mm for Amatex 20 and 12 mm for Composition B. The gages extended from 25 to 76 mm beyond the tops of the blocks in both cases. Gage spacings in the completed targets are given in a later subsection of this section.

Casting

The casting operations were performed at Los Alamos Scientific Laboratory (LASL). Ingredients and casting parameters for each study material were suggested by J. Hershkowitz of Arradcom and A. Popolato of LASL; that information is available from LASL. Procedures related to the gages and targets were determined jointly by SRI and LASL personnel and are described below. The casting operations and subsequent quality testing were directed by A. Torres, LASL, with J. T. Rosenberg of SRI observing the Composition B casting.

Each gage block was mounted, gages up, on the horizontal base plate of an oversized cylindrical casting mold. The molten explosive was poured slowly into the molds using a trough to deflect it away from the gages.

Care was taken to avoid either disturbing the gages or allowing bubbles to form near them. Each mold was filled to a depth of about 9-in, covered by a thermostatically-controlled heating panel, and cooled according to a programmed cycle previously developed for each material at LASL. The less uniform material was machined from the tops and sides of the casting to achieve the final target dimensions. Approximately 4 in of material was removed from the tops and 1 to 3 in from the diameter of the castings. Final target dimensions are given later in this section.

Study Materials

All targets were x-rayed at LASL and one target of each material was cored to check the quality of the casting and to determine material uniformity and density. The x-rays revealed neither cracks or voids within the charges nor distortions of the gages. However, because of the relatively large dimensions of the cylindrical targets(about 8-in in diameter by 5-in in height) the minimum flaw size detectably by x-raying may be large. Because of the large ratio of explosive to gage thickness in the x-ray path and the similarity in x-ray absorption cross sections of aluminum and HE, it was difficult to obtain resolvable images of the embedded gages. It was, therefore, necessary for LASL to decrease the diameter of the Amatex 20 targets from 9 to 8-in and that of the Composition B targets from 8 to 7-in to obtain images of the long dimension (25.5 mm) of the gage elements; images through the width and thickness were not obtained.

Estimates of the compositions and densities of each of the study materials were obtained by LASL by removing and examining a series of cores from one specimen of each material. The coring patterns are shown in Figures 4 and 5; the composition and density measurements are given in Tables 1 and 2.

Finished Dimensions

The targets were solid cylinders of HE with a smooth machine finish on the exterior surfaces. The rear of the embedded gage blocks extended about 12 mm beyond the back surface of the HE. The HE targets for both Amatex 20 and Composition B were nominally 127 mm (5.00 in) in height;

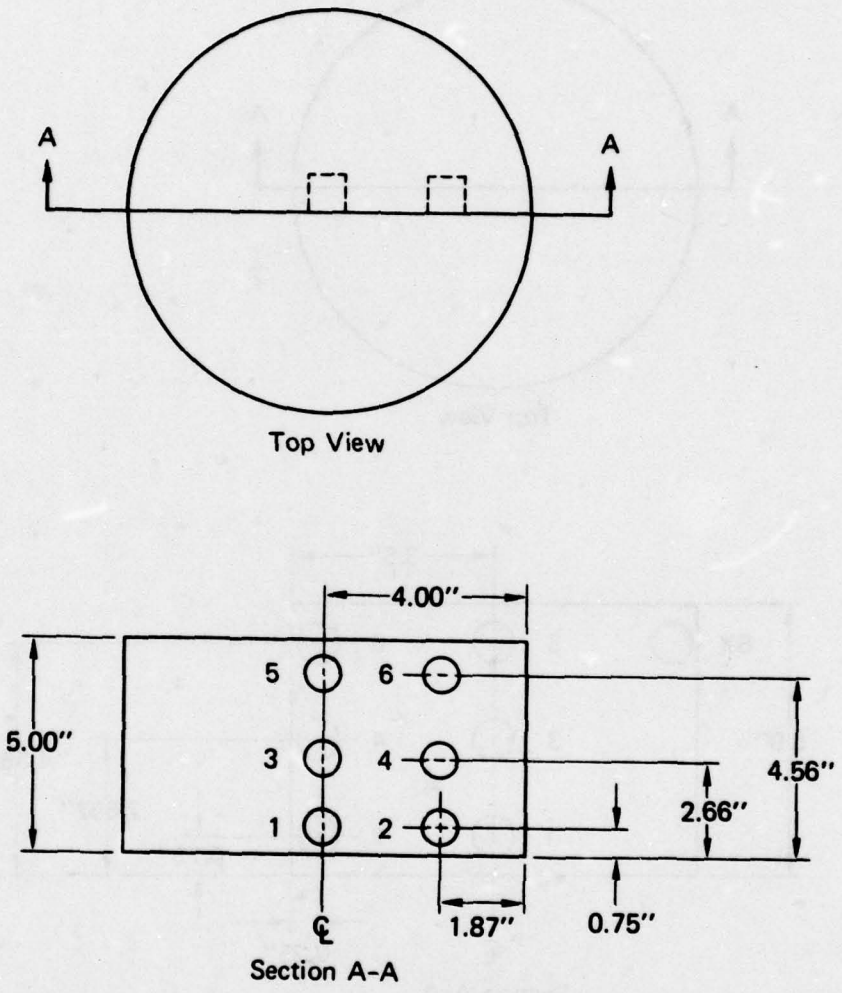

FIGURE 4 CORE SAMPLE PATTERN IN AMATEX 20 CASTING

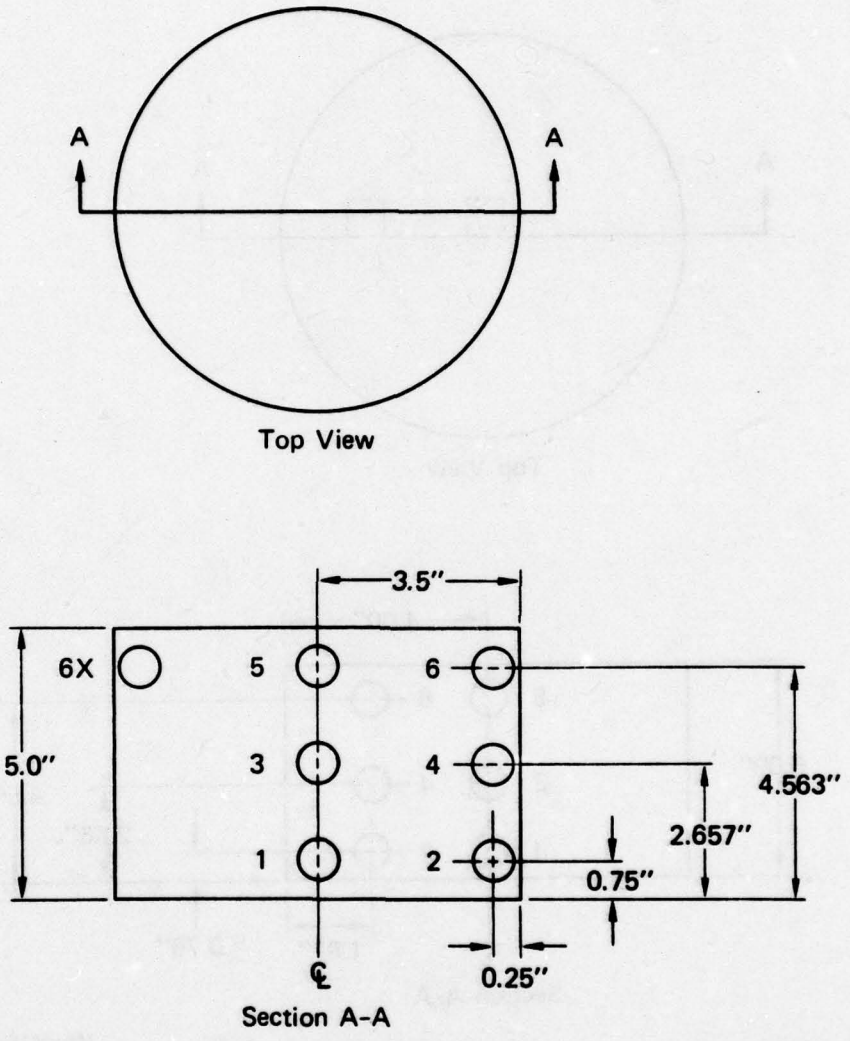

FIGURE 5 CORE SAMPLE PATTERN IN COMPOSITION B CASTING

Table 1

COMPOSITION AND DENSITY OF AMATEX 20 TARGETS*

Core No.	Density (g/cm^3)	Composition		
		AN	RDX	TNT†
1	1.643	40.15	19.50	40.35
2	1.648	40.21	19.88	39.91
3	1.592	38.87	20.23	40.90
4	1.607	38.91	20.39	40.70
5	1.587	36.99	20.73	42.28
6	1.598	37.73	20.32	41.95
Average:	1.613	38.84	20.18	41.02
Std Dev:	0.024	1.20	0.39	0.84

*Private communction, A. Torres, Los Alamos Scientific Laboratory, Los Alamos, NM, 87545, 14 July, 1977.

†Obtained by difference; includes the small quantity of wax used in Composition B,

Table 2

COMPOSITION AND DENSITY OF COMPOSITION B TARGETS*

Core	Density (g/cm^3)	Composition (wt%) RDX	TNT†
1	1.715	64.47	35.53
2	1.719	65.34	34.66
3	1.719	65.32	34.68
4	1.718	63.32	36.68
5	1.716	65.81	34.19
6	1.717	62.63	37.37
6x	1.716	63.19	36.81
Average	1.717	64.30	35.70
Std Dev	0.002	1.16	1.16

*Private communication, A. Torres, Los Alamos Scientific Laboratory, Los Alamos, NM 87545, 18 September 1978.

†Obtained by difference; includes the small quantity of wax used in Composition B.[1]

the nominal diameters of the targets were different, however, being 203 mm (8.00 in) for Amatex 20 and 178 mm (7.00 in) for Composition B. The back (exposed) surfaces of the gage blocks were parallel to the front surfaces of the targets to within ± 0.25 mm (0.01 in) for Amatex 20 and ± 0.50 mm (0.02 in) for Composition B.

Gage separations in the wave propagation direction were determined primarily from measurements of the gage blocks before HE casting and were confirmed by spot checking the LASL x-rays and by examining the linearity of the observed detonation trajectory calculated on the basis of the gage-block gage spacing. The x-rays give an image of the center of mass of the gage elements projected along their long dimension and could, in principle, be used for the primary gage separation determination. However, because of the difficulty in resolving the gage images on the x-rays this was not convenient. Neither the x-ray measurements nor the shapes of the shock trajectories revealed any cases in which relative gage separations changed after casting.

Each target contained two sets of identically spaced gages with six gages per set in the case of Amatex 20 (see Figure 3) and five gages per set for Composition B. One set of gages on each Amatex 20 gage block was displaced 1.58 mm (0.062 in) farther from the block than the other to simplify identification on the x-rays and photographs of corresponding gages from different gage sets. This offset method was not used with the Composition B gage blocks. Gage separations and distances from front and back target boundaries are given per gage set in Table 3. Note that gages are numbered consecutively across the block from end to end; for example, gages 1 and 12 (or 1 and 10 for Composition B) are the longest gages, gages 2 and 11 are the next longest, and so on (refer to Figure 3). Gages 1 and 12 (or 1 and 10 in Composition B) are the end gages and are the same length (except for the 1.58 mm offset in Amatex 20). Because they are the longest gages, these end gages are the first to sense the detonation wave.

Table 3

GAGE SEPARATIONS IN THE WAVE PROPAGATION DIRECTION[a]

Element[b] Pair	Separation (mm)	
	Amatex 20[c]	Composition B[c]
Target front face/gage 1	31.7[d]	31.7
Gage 1/gage 2	12.7	12.7
Gage 2/gage 3	12.7	12.7
Gage 3/gage 4	6.4	12.7
Gage 4/gage 5	6.4	12.7
Gage 5/gage 6	12.7	(f)
Gage 6[f]/gage block	25.4	25.4[f]

[a] Each target contained two identical gage sets; the spacings given here are applicable to both sets.

[b] An element is either a gage or the front or back surface of the HE target.

[c] Spacings are estimated to be accurate within 1%.

[d] 30.1 mm in other gage set because of offset described in text.

[e] 27.0 mm in other gage set because of offset described in text.

[f] There are five gages per set for Composition B; the last gage is gage 5.

Experimental Results

Six experiments were performed using three replicate targets of each study material. The objective was to obtain at least one reliable set of Lagrange particle velocity histories (for use in the Lagrange analysis) during self-sustaining planar detonation in each material. Experiment numbers, study materials, and HE drivers (see Figure 2) are listed in Table 4.

The experiments were performed at SRI's remote test site, CHES, in two series separated by several months. Experiments 1 and 2, with Amatex 20 targets, were fired in the first series; Experiments 3-5 with Composition B targets and Experiment 6 with an Amatex 20 target were fired in the second series of tests. Particle velocity records were obtained in all experiments. Experimental records of interest for analysis or experiment interpretation were reduced to particle velocity histories; they are presented in Figures 6-9. These profiles are the primary experimental results obtained in this program. The Amatex 20 data in Figures 7a and 7b from Experiment 6 and the Composition B data in Figure 9b from Experiment 5 were used in the Lagrange analyses presented in the following chapter.

Discussion

Measurement Interpretation and Reliability

Because of the geometrical constraints imposed by EPV gage operation and analysis, each of the reported particle velocity profiles is strictly valid only while the corresponding gage and leads experienced planar flow. Planar flow ceases either when edge effects from the lateral boundaries of the target reach the gage elements or when the detonation reaches the near surface of the gage block, which ever occurs first. Edge effects limited the first gages and the detonation arrival limited the last. The planar flow test time can be further reduced by wave-front curvature or other imperfections arising in the plane wave lens and driver system. We have conservatively estimated the average useful profile duration from first motion to be about 3 μs for Amatex 20 (Figures 6 and 7) and less than 2 μs for Composition B (Figures 8 and 9). The differences are due primarily to the smaller diameter of the Composition B targets.

Table 4

EXPERIMENTS AND STUDY MATERIALS

Experiment Number*	Study Material	HE Driver† and Thickness
1	Amatex 20	TNT, 1 in
2	Amatex 20	TNT, 1 in
3	Composition B	--
4	Composition B	--
5	Composition B	--
6	Amatex 20	TNT, 1 in + Amatex 20 (2 in)

*Full number is given preceded by 5414-2-

†8-in diameter cylindrical pads.

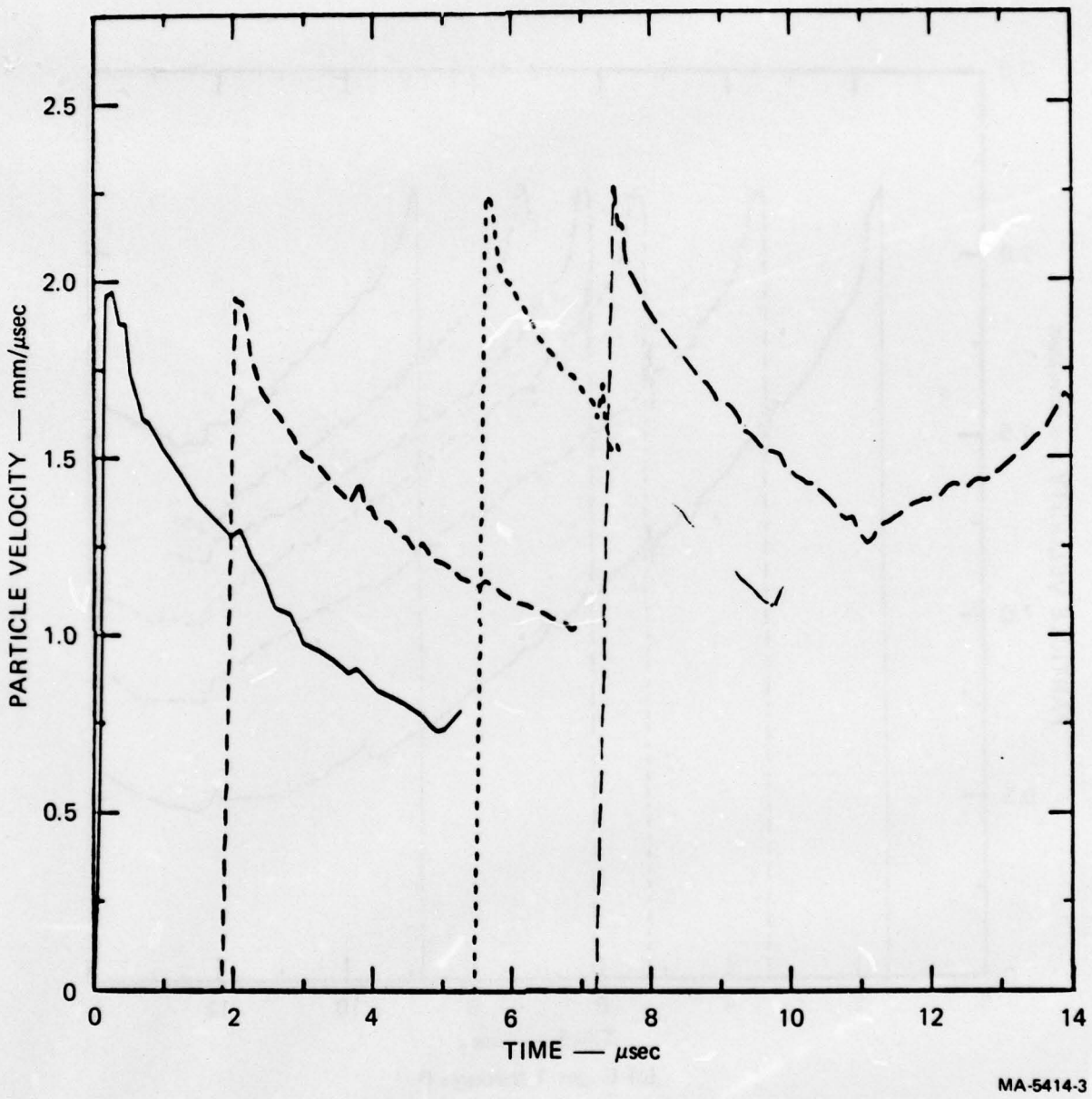

FIGURE 6 PARTICLE VELOCITY HISTORIES IN DETONATING AMATEX 20, EXPERIMENT 1, GAGES 1, 2, 5, AND 6

The recorded histories indicate that buildup to steady detonation is completed between gages 2 and 5 (see text).

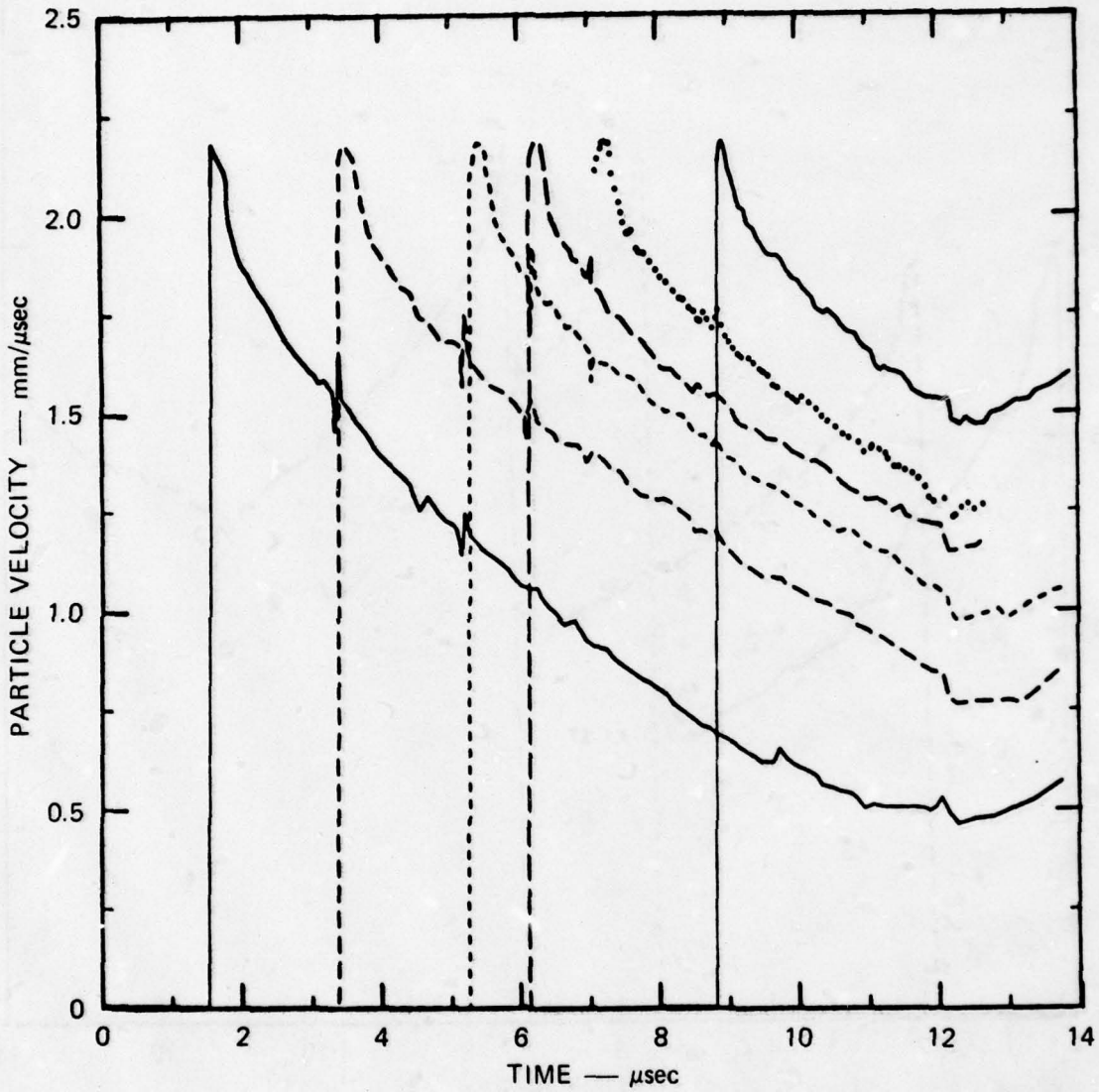

(a) Gages 1 through 6

MA-5414-4

FIGURE 7 PARTICLE VELOCITY HISTORIES IN DETONATING AMATEX 20, EXPERIMENT 6

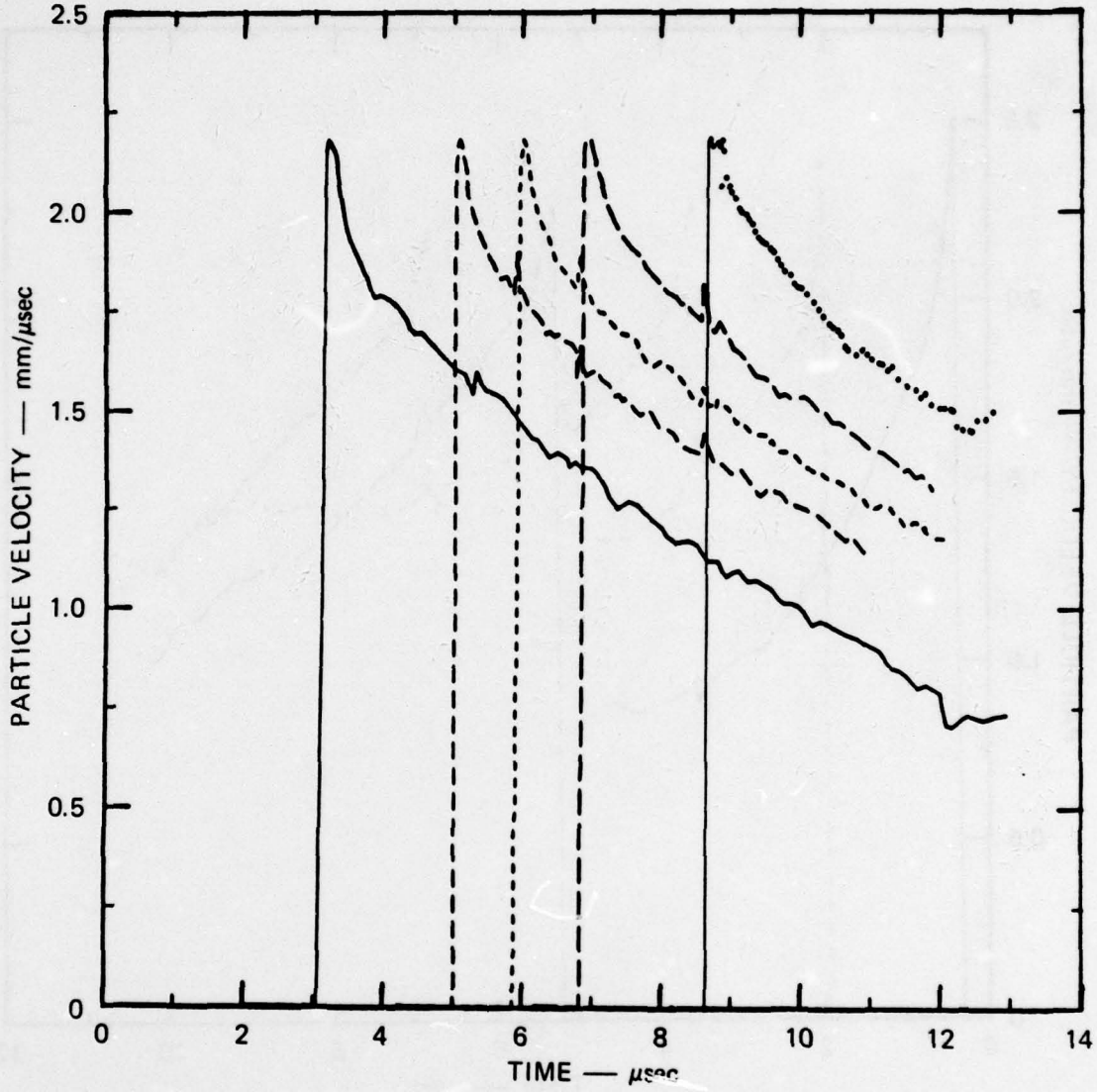

(b) Gages 7 through 11

MA-5414-5

FIGURE 7 PARTICLE VELOCITY HISTORIES IN DETONATING AMATEX 20, EXPERIMENT 6 (Concluded)

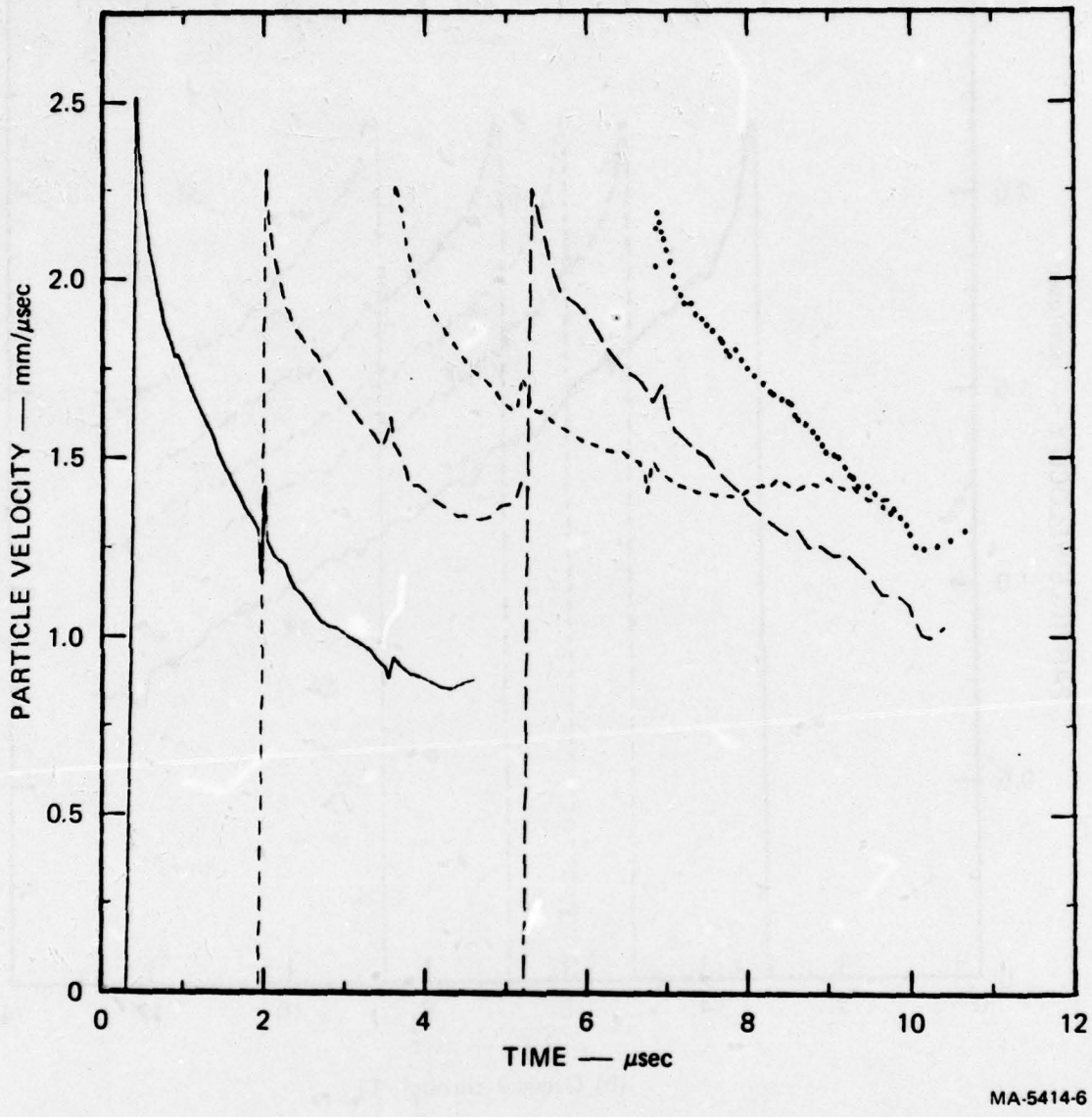

FIGURE 8 PARTICLE VELOCITY HISTORIES IN DETONATING COMPOSITION B, EXPERIMENT 4, GAGES 6 THROUGH 10

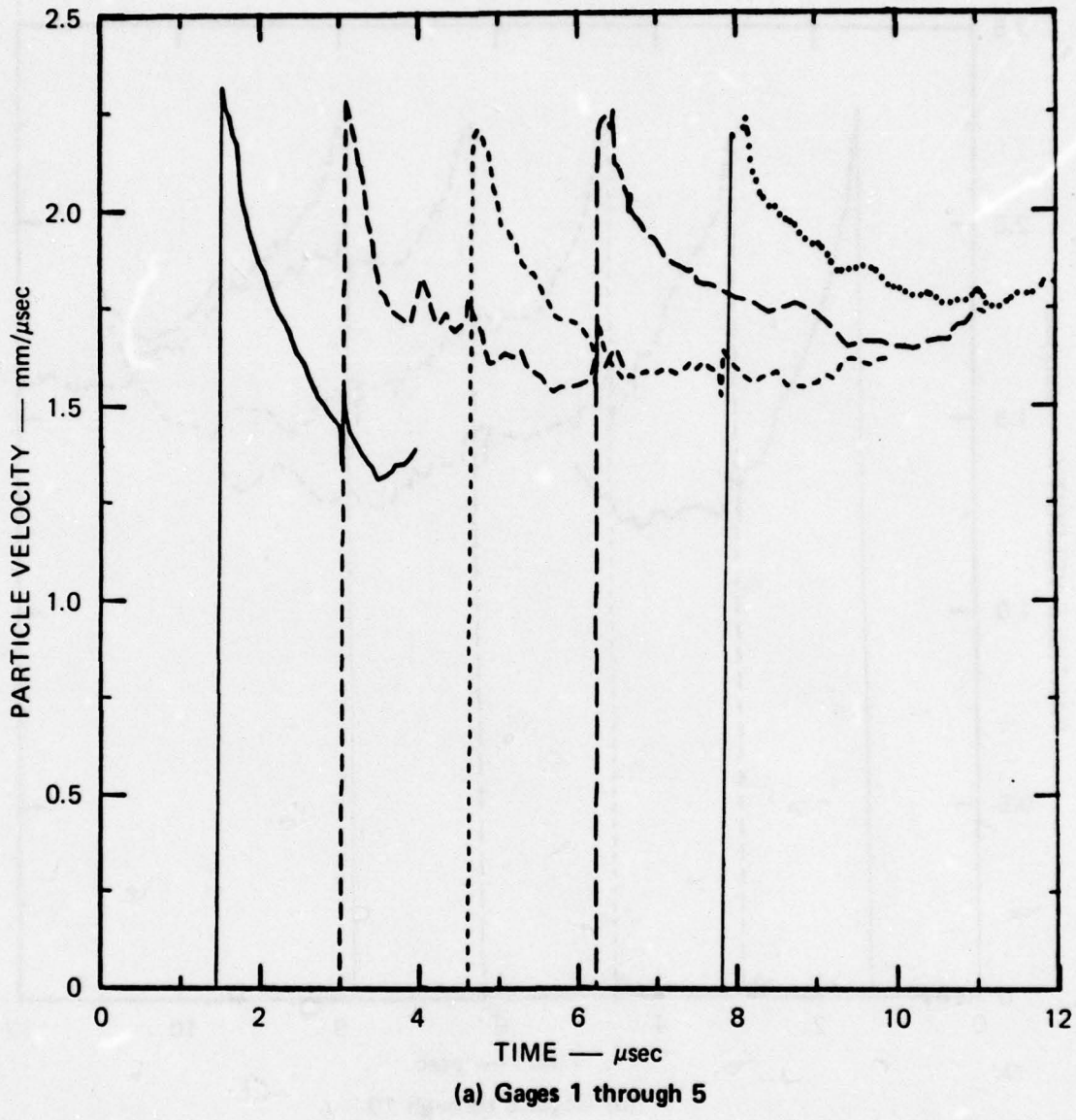

FIGURE 9 PARTICLE VELOCITY HISTORIES IN DETONATING COMPOSITION B, EXPERIMENT 5

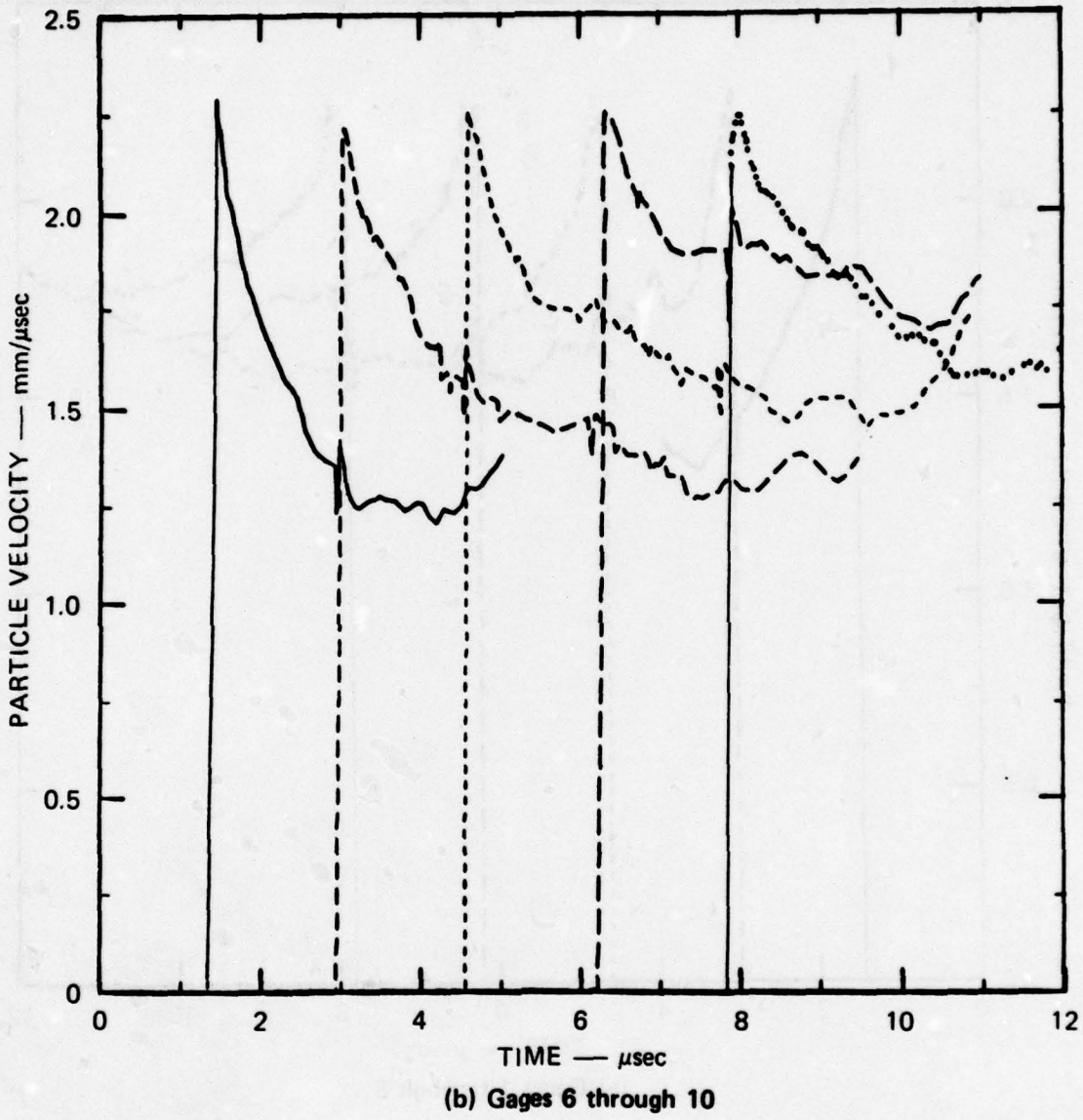

(b) Gages 6 through 10

MA-5414-8

FIGURE 9 PARTICLE VELOCITY HISTORIES IN DETONATING COMPOSITION B, EXPERIMENT 5 (Concluded)

Direct current voltage calibrations of the oscilloscopes were performed after both series of shots, as described earlier. However, in reducing the data from the second series of shots, we discovered that the calibrated voltage steps recorded on the Tektronix 500 series oscilloscopes had systematic errors not present on the calibration records from the 7000 series scopes. The problem was traced to differences in the response times of the two series of oscilloscopes to stepped voltages applied under our calibration conditions. Since the 7000 series calibrations were reliable and because one of these oscilloscopes had been used on each of the gages in one gage set in Experiment 6, we were able to obtain the self-consistent set of profiles for Amatex 20 shown in Figure 7b. The recorded peak particle velocities signals, which agreed to within ± 1.5%. were averaged and used as a voltage step to calibrate the rest of the oscilloscopes for all experiments in the second series. This procedure was not applied to data from the first series.

The particle velocity profiles in both study materials show small glitches at the instant a downstream gage entered the detonation front. This is attributed to a slight resistive coupling of the gage circuits in question through the conductive detonation front, not to a real oscillation in the particle velocity history. We therefore recommend that these glitches be smoothed out for the purposes of flow analysis. Determination of the source of the shape deviations observed in the late-time particle velocity profiles recorded in Composition B, Figures 8 and 9, was beyond the scope of program. Possibilities include differences in the time at which planar flow conditions terminated at the various gage elements or leads, measurement artifacts caused by conductivity in the target, target construction defects, or real differences in the flow at these Lagrange coordinates. Because of this uncertainty, we place no confidence in the Composition B profiles beyond about 1 μs. Later supporting experiments might, however, extend this interval considerably.

Study Material Response

The results of Experiments 1 and 2 were similar and are typified by the profiles in Figure 6. Two important features of both experiments were the growth in peak particle velocity between gages 2 and 5 and the fact that the profiles recorded by the last two gages were essentially the same. The growth in peak particle velocity may be an artifact of the voltage calibration methods used in the first experiment series; however, we think it is more likely that it is real and that it is caused by the initiation of detonation in Amatex 20 taking longer than expected. In either case, self-sustaining detonation was recorded by the last two gages entering the flow. Examination of those two particle-velocity histories led to the conclusion that self-sustaining detonation in Amatex 20 propagates as a steady-state wave supported by the reaction of the ammonium nitrate.

In the second series of experiments, an additional 2-in-thick pad of Amatex 20 provided by LASL was sandwiched between the driver used in Experiments 1 and 2 and the Amatex target. The purpose was to lengthen the time that it took the detonation wave to reach the gages so that all the gages would be located in the self-sustaining detonation region. This Amatex 20 charge and three Composition B charges were fired successfully. Examination of the Amatex 20 histories from Experiment 6 (Figure 7), the Composition B histories from Experiment 5 (Figure 9), and one set of histories from Experiment 4 (Figure 8) shows that self-sustaining detonation was obtained in both explosives and that the particle velocity attained its maximum value at the wave front. Comparison of the particle velocity histories behind the shock front in Composition B shows that the rarefactive flow is unsteady and exhibits features expected of a nonreactive Taylor wave. However, comparison of the particle velocity histories behind the shock front in Amatex 20 shows that the rarefaction flow essentially attains a steady-state condition. This requires that the flow behind the wave front in Amatex 20 was supported by the reaction of the ammonium nitrate. Detonation velocities and peak particle velocities in Amatex 20 and Composition B determined from these observed particle velocity histories are given in the next chapter.

Conclusions and Recommendations

The experimental techniques, and in particular the new gage emplacement method, worked well and provided new and useful data on self-sustaining detonation in both study materials. The data return was nearly 100% and the information appears reliable. We believe, however, that further refinements in the Lagrange gage techniques used in this work are possible and could lead to improvements in three areas: (1) the duration of planar flow at the gages and hence the extent of the release process available for study, (2) the accuracy of the measurements, and (3) the confidence that can be placed in multiple internal gage measurements. Recommendation involving target construction and measurement methods, signal measurement techniques, and supporting experiments are listed below.

Target Construction and Measurement

The use of larger diameter targets would increase test time by delaying the termination of planar flow conditions at the gage elements. The diameters of both types of targets in this work were limited by the difficulty in resolving x-ray gage images needed for post-casting determination of gage locations. Three alternative approaches for determining gage locations in the larger targets should be examined. These are (1) to perform sufficient destructive and nondestructive tests on controls so that x-ray measurement on experimental targets are unnecessary,* (2) to construct the targets with outer sections removable during x-raying, and (3) to examine methods for increasing gage resolution on the x-rays. Planar test time at the gages also can be increased either by (1) decreasing the number of gages per target or (2) by redesigning the gage layout within the target for greater gage clustering in the center,or by both (1) and (2).

Small increases in the gage dimensions, particularly the width, are recommended to decrease electrical resistance and thereby reduce gage-gage interactions or gage shunting by the conductive reaction products.

---

*Independent confirmation of gage locations is available after the experiment from a distance-time plot of the detonation trajectory.

Increased width would also provide additional mechanical strength for handling and casting. Finally, we recommend improving the alignment of the gage elements with the plane of the flow. This can be accomplished by modifying the gage-block design, particularly the back surface, and the target machining techniques to increase parallelism between the target front surfaces and the gage-block back surfaces.

Signal Measurement Techniques

We recommend that the present method of determining the magnetic field from the current in the Helmholtz coils be supplemented with direct measurements of the field. The use of Hall probes (possibly sacrificial) for this purpose could provide increased measurement accuracy and confidence in the technique. Experimental precision could also be increased by improving the oscilloscope voltage calibration methods. We suggest that methods for performing ac calibrations of the recording circuits and instrumentation be developed.

Support Experiments

The scope of this program has not permitted supporting experiments to verify the assumptions required to design the experiments. It would be desirable in future work to experimentally examine the following questions: the necessity of using expensive differential signal recording methods; the effectsof upstream gages on subsequent chemical and mechanical processes in the flow; the degree of electrical coupling between gage circuits; and the cumulative effects of the conductive reaction products on the measurement. Experiments to examine most of these are straightforward. The latter might be examined, for example, by comparing measurements of the velocity of an interface between HE and a transparent witness-window material obtained using both EPV gages and an optical method.

4. LAGRANGE ANALYSIS

Procedure and Results

Lagrange analysis provides a quantitative description of the one-dimensional flow produced in a shock or detonation wave experiment from a set of stress or particle velocity gage histories recorded along different particle paths. The flow variables are generated by integrating the equations of motion with flow derivatives estimated from the data supplied by the gage records. The momentum equation (5) gives dynamic Lagrange* (p,u) relationships between pressure and particle velocity, and the continuity equation (4) gives dynamic Lagrange (v,u) relationships between specific volume and particle velocity. The elimination of u between these (p,u) and (v,u) relationships gives the corresponding Lagrange (p,v) relationships.

The sets of particle velocity histories for detonating Amatex 20 (Figures 7a and 7b) and those for detonating Composition B (Figure 9) were the basis for the Lagrange analysis performed here. The GUINSY code[11] written by L. Seaman of SRI International was used to carry out this analysis. Before the data in Figures 7a, 7b, and 9 were used, they were smoothed as recommended in the preceding section, by removing obvious artifacts, such as the coupling among gages.

The smoothed (u,t) profiles for Amatex 20 generated from the (u,t) records in Figure 7a are shown in Figure 10, and the calculated stress-histories, Lagrange (p,u) and Lagrange (p,v) relationships are shown in Figures 11-13. The smoothed histories and calculated Lagrange plots for detonating Amatex 20 generated from the (u,t) records in Figure 7b are shown in Figures 14-17. The smoothed histories and calculated Lagrange

*That is, along particle paths.

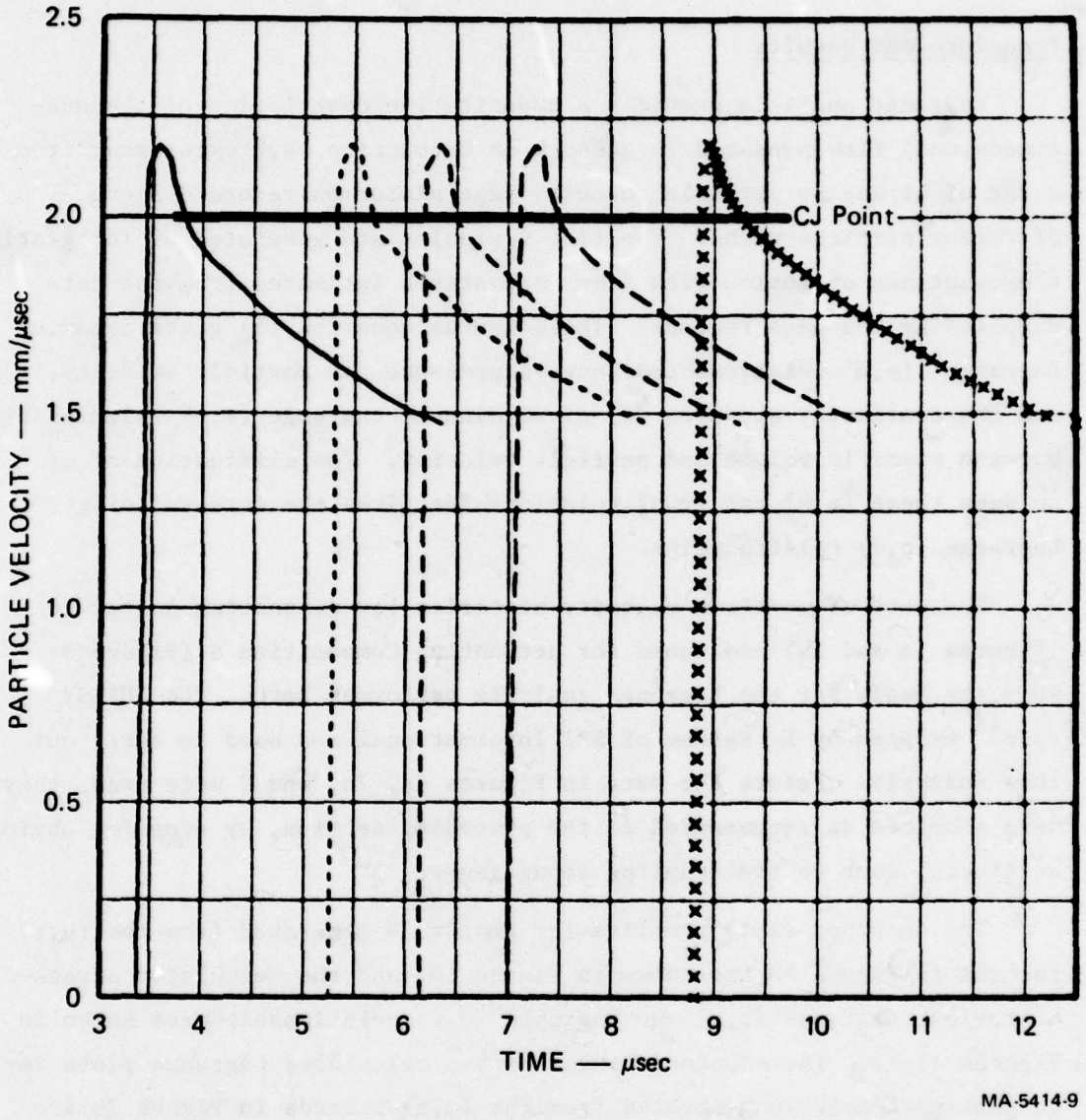

FIGURE 10 SMOOTHED PARTICLE VELOCITY HISTORIES IN DETONATING AMATEX 20 (EXPERIMENT 6, GAGES 2 THROUGH 6) USED IN LAGRANGE ANALYSIS

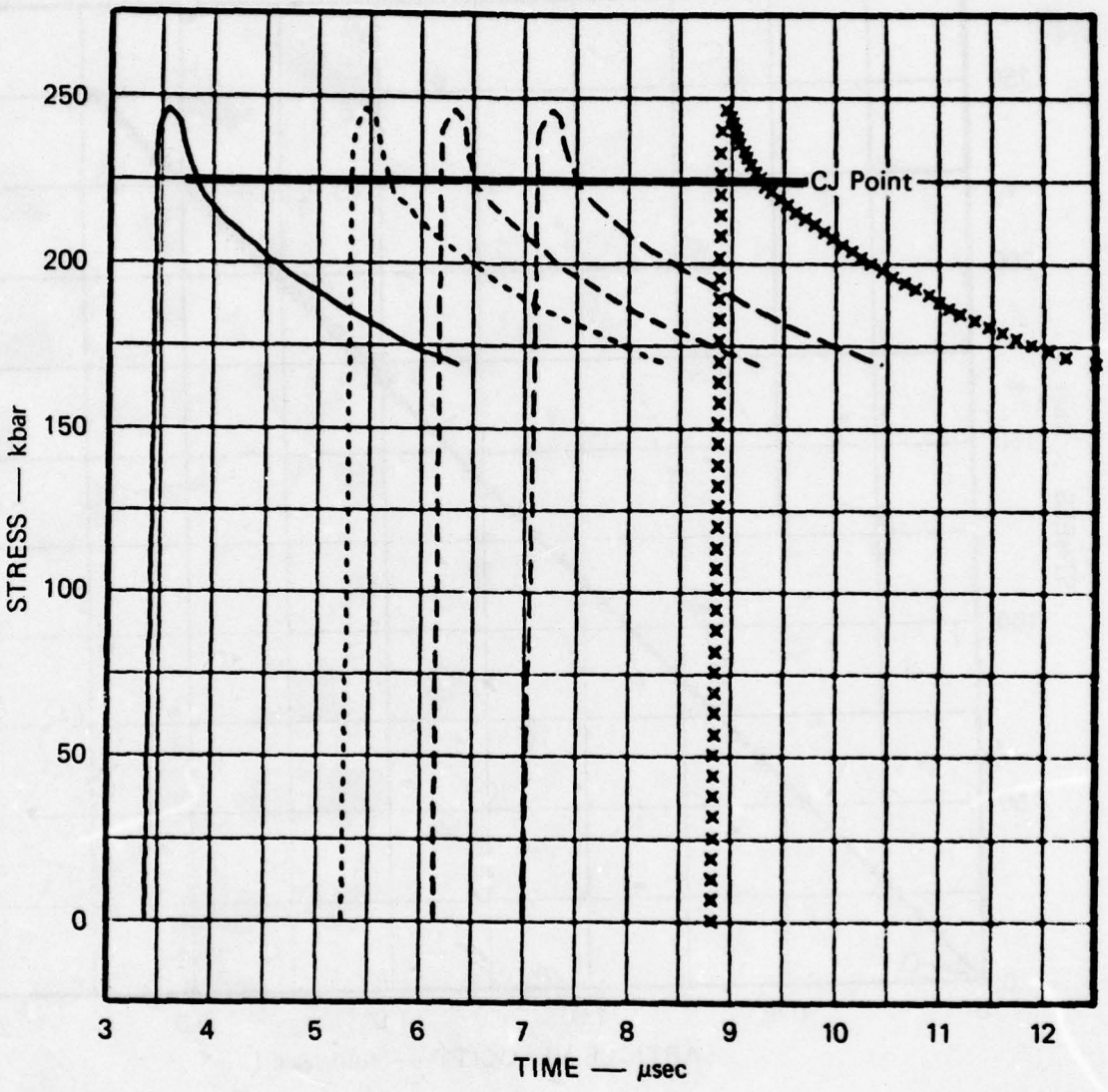

FIGURE 11 LAGRANGE STRESS HISTORIES AT THE GAGE POSITIONS IN DETONATING AMATEX 20 CALCULATED FROM THE PARTICLE VELOCITY HISTORIES SHOWN IN FIGURE 10

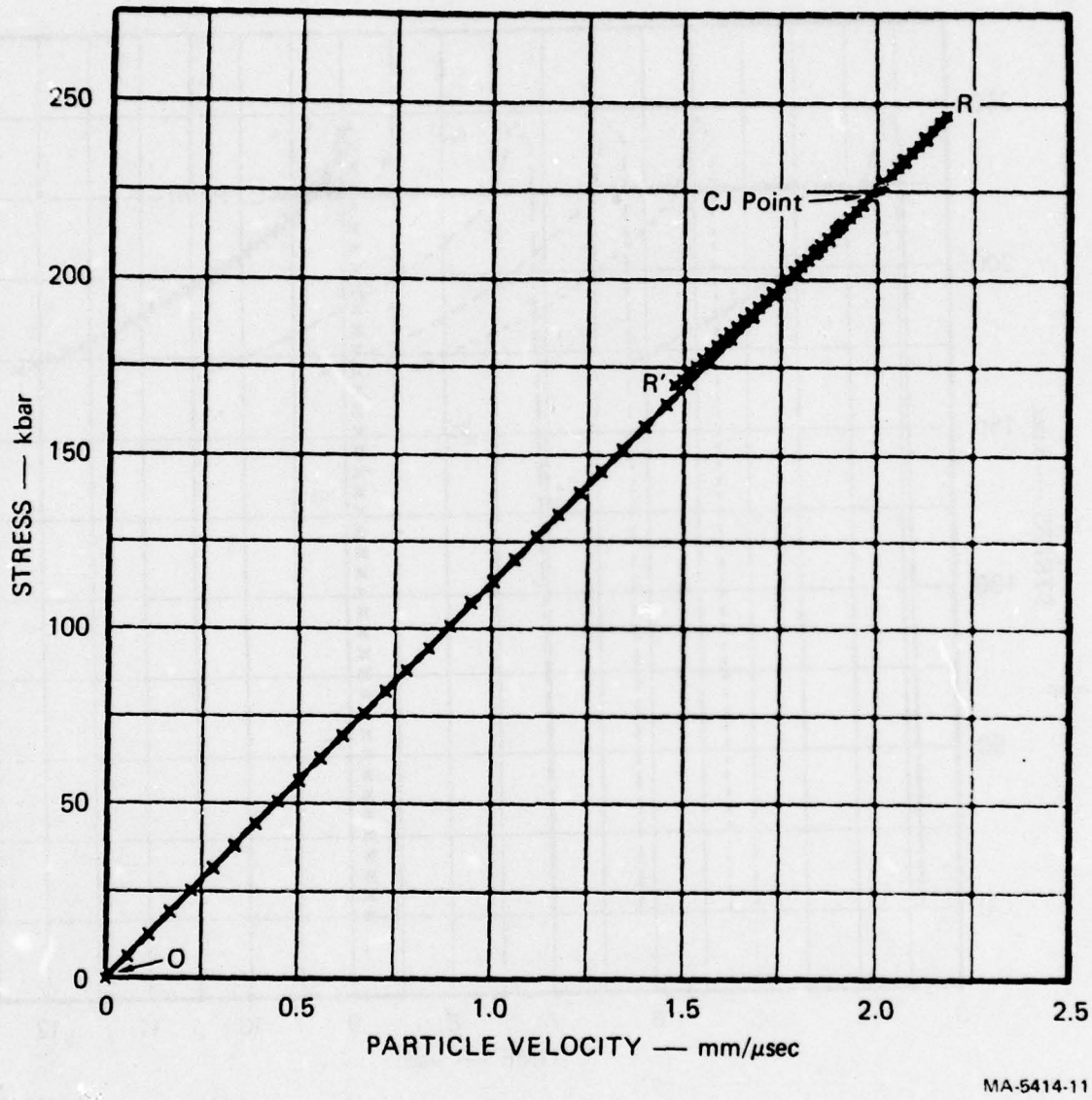

FIGURE 12 LAGRANGE STRESS—PARTICLE-VELOCITY LOAD-UNLOAD PATHS AT THE GAGE POSITIONS IN DETONATING AMATEX 20 CALCULATED FROM THE PARTICLE VELOCITY HISTORIES SHOWN IN FIGURE 10

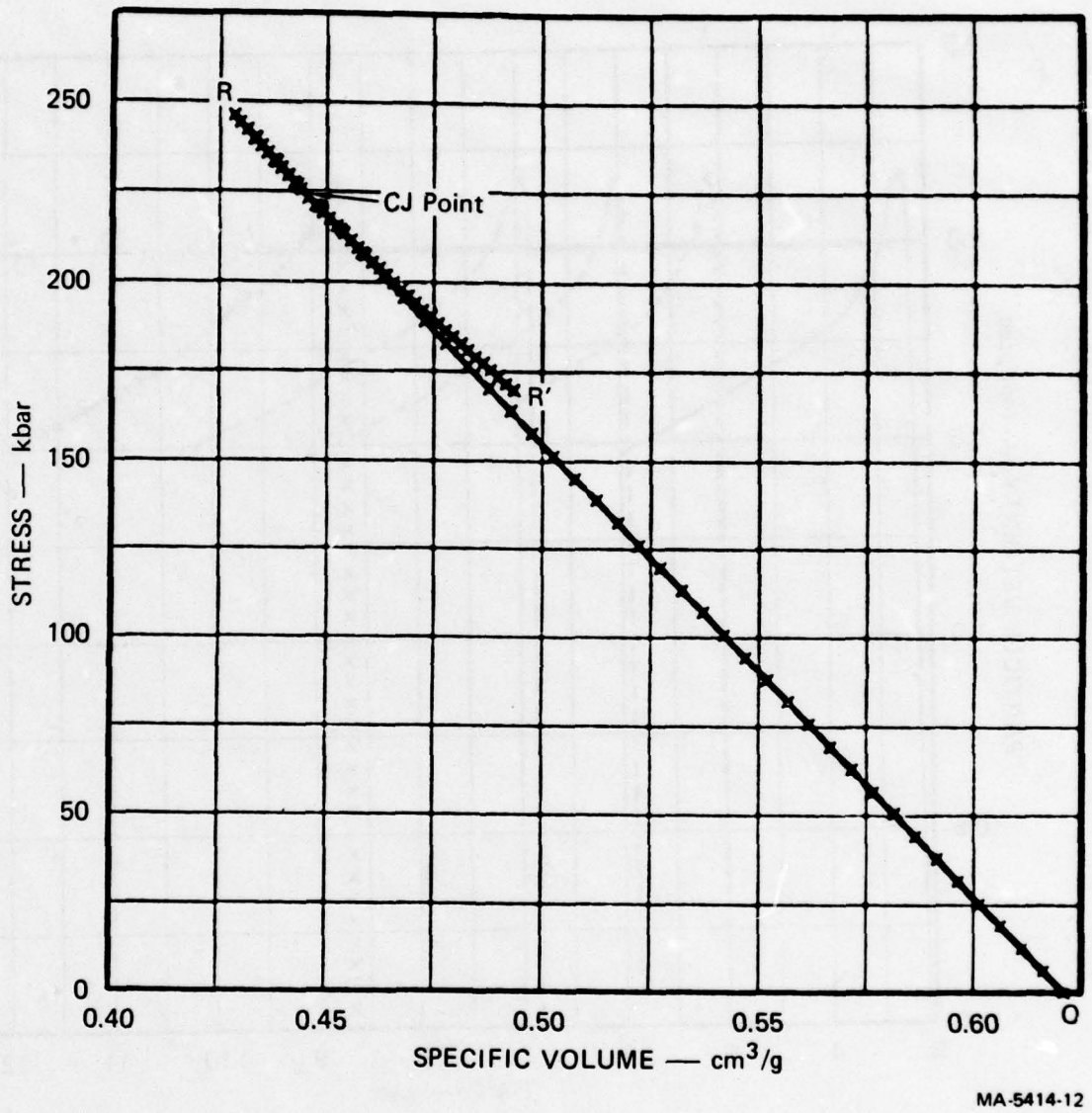

FIGURE 13 LAGRANGE STRESS—SPECIFIC-VOLUME LOAD-UNLOAD PATHS AT THE GAGE POSITIONS IN DETONATING AMATEX 20 CALCULATED FROM THE PARTICLE VELOCITY HISTORIES SHOWN IN FIGURE 10

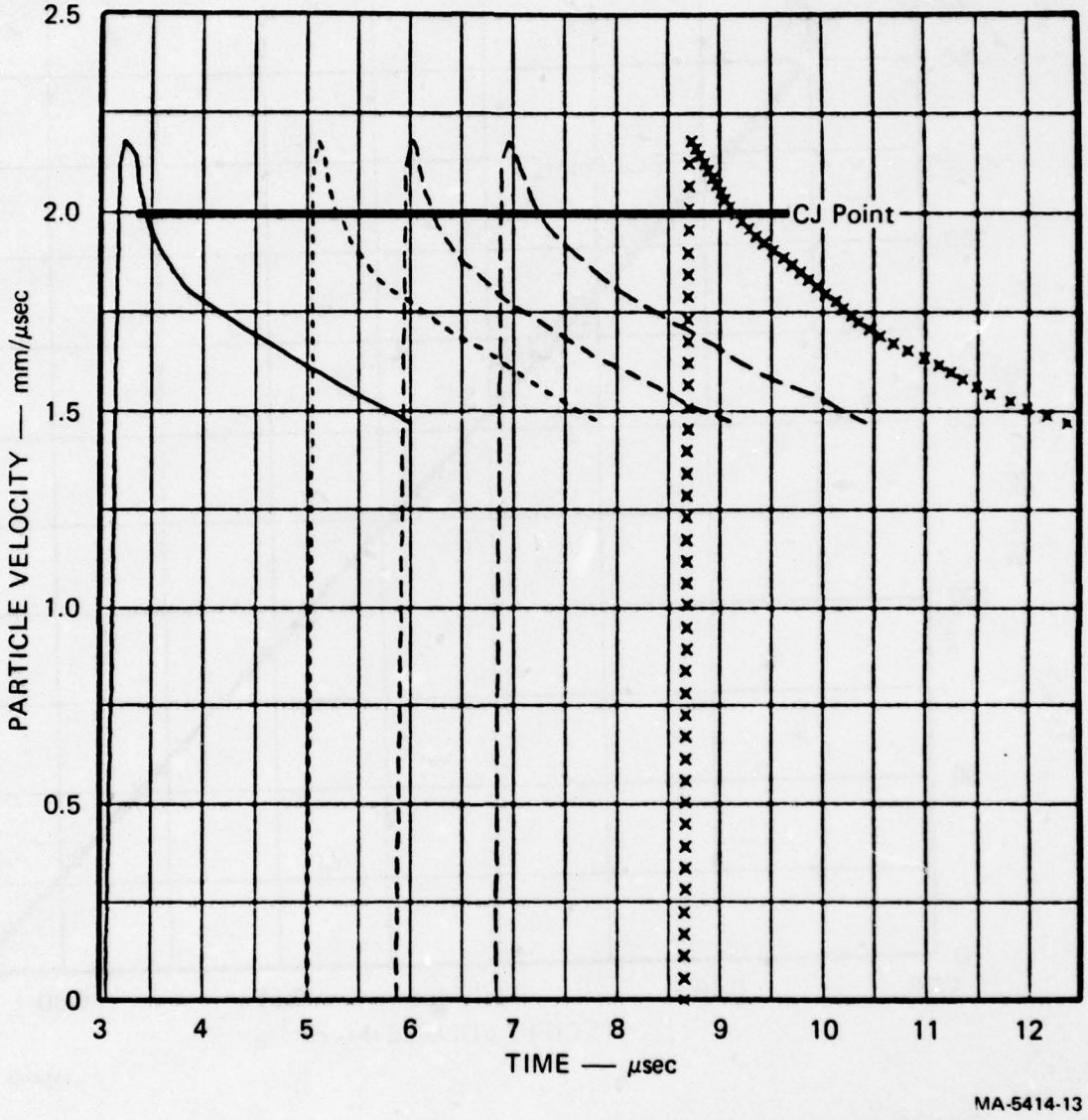

FIGURE 14 SMOOTHED PARTICLE VELOCITY HISTORIES IN DETONATING AMATEX 20 (EXPERIMENT 6, GAGES 7 THROUGH 11) USED IN LAGRANGE ANALYSIS

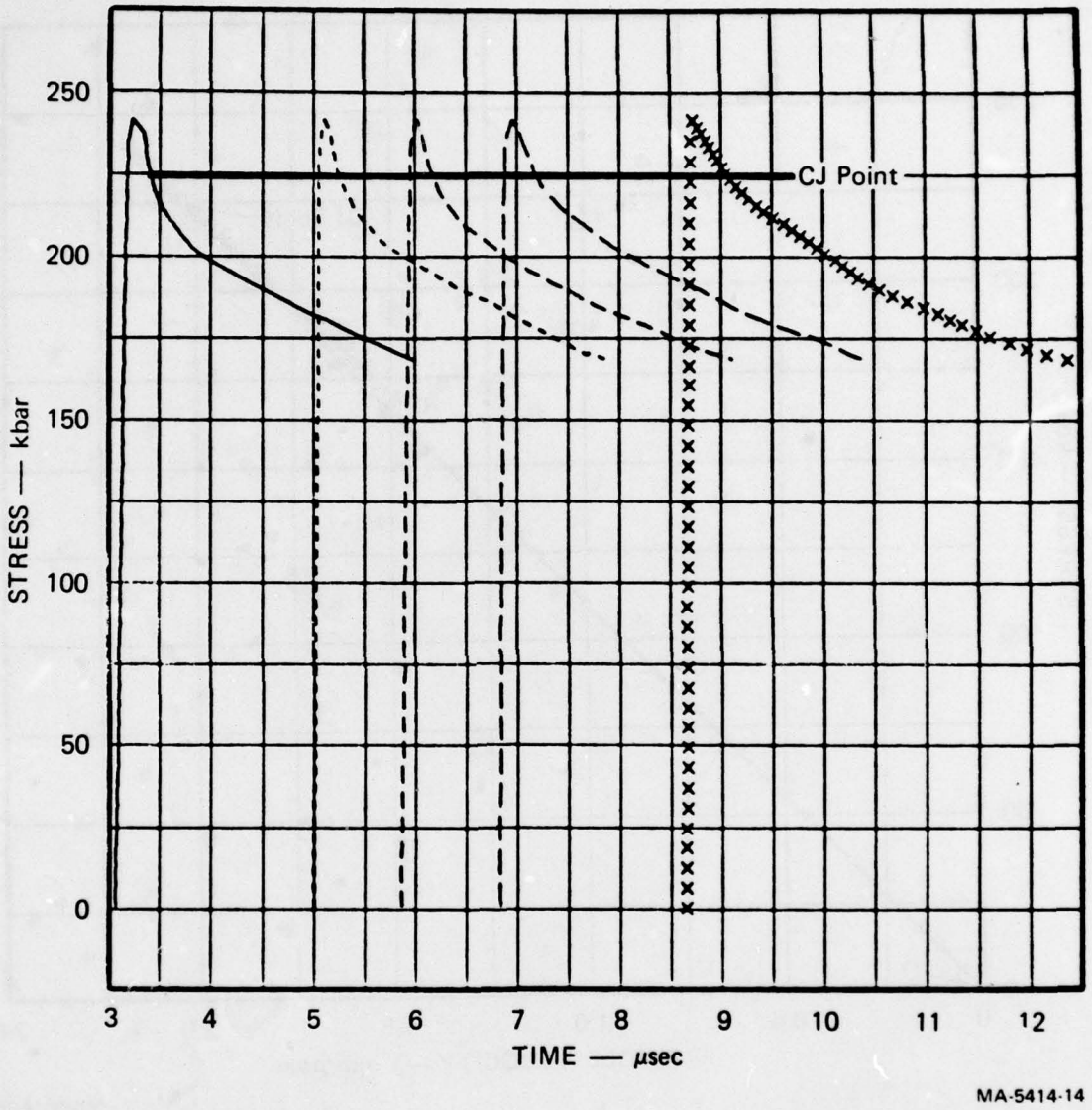

FIGUR E 15 LAGRANGE STRESS HISTORIES AT THE GAGE POSITIONS IN DETONATING AMATEX 20 CALCULATED FROM THE PARTICLE VELOCITY HISTORIES SHOWN IN FIGURE 14

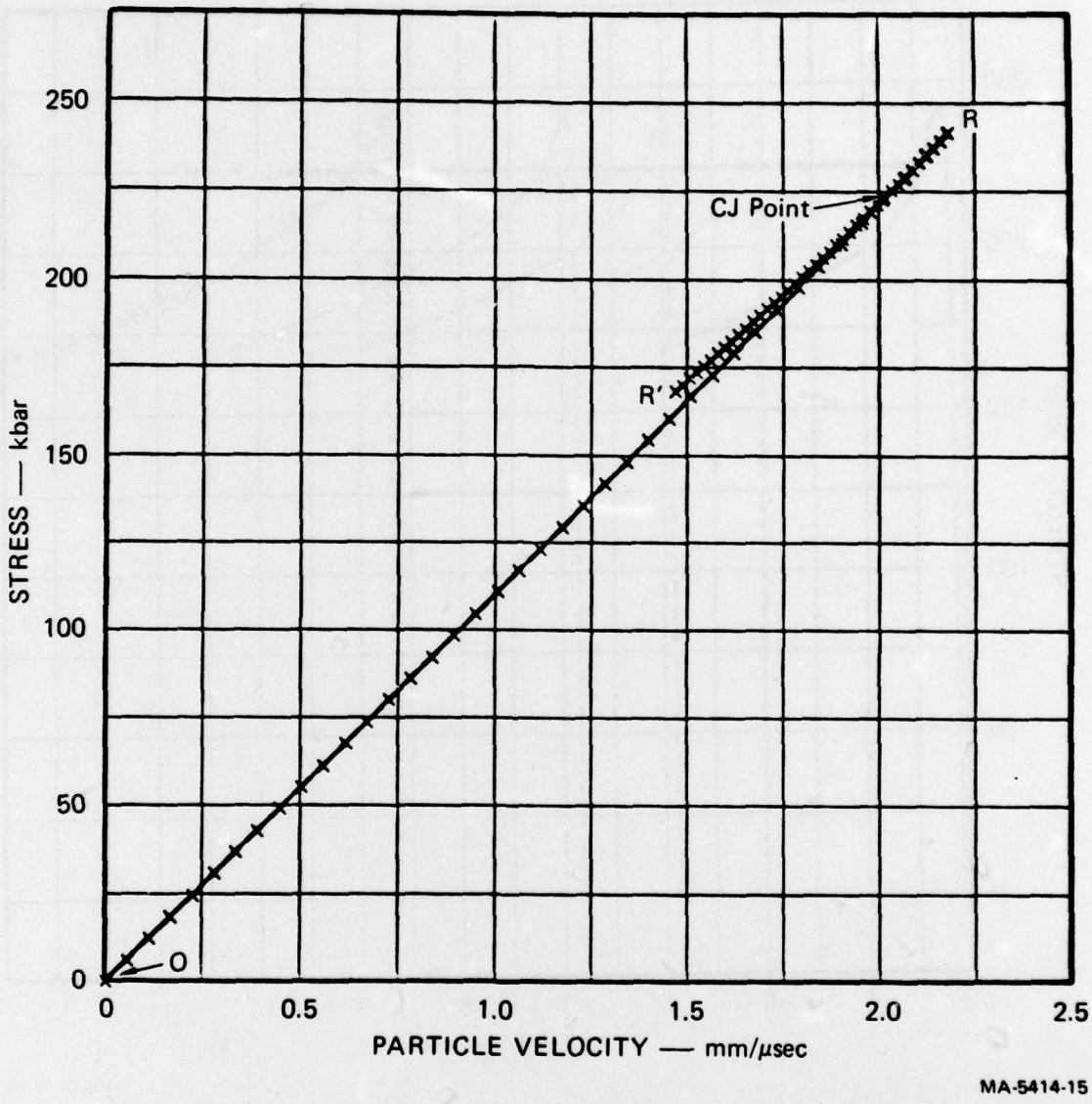

FIGURE 16 LAGRANGE STRESS—PARTICLE-VELOCITY LOAD-UNLOAD PATHS AT THE GAGE POSITIONS IN DETONATING AMATEX 20 CALCULATED FROM THE PARTICLE VELOCITY HISTORIES SHOWN IN FIGURE 14

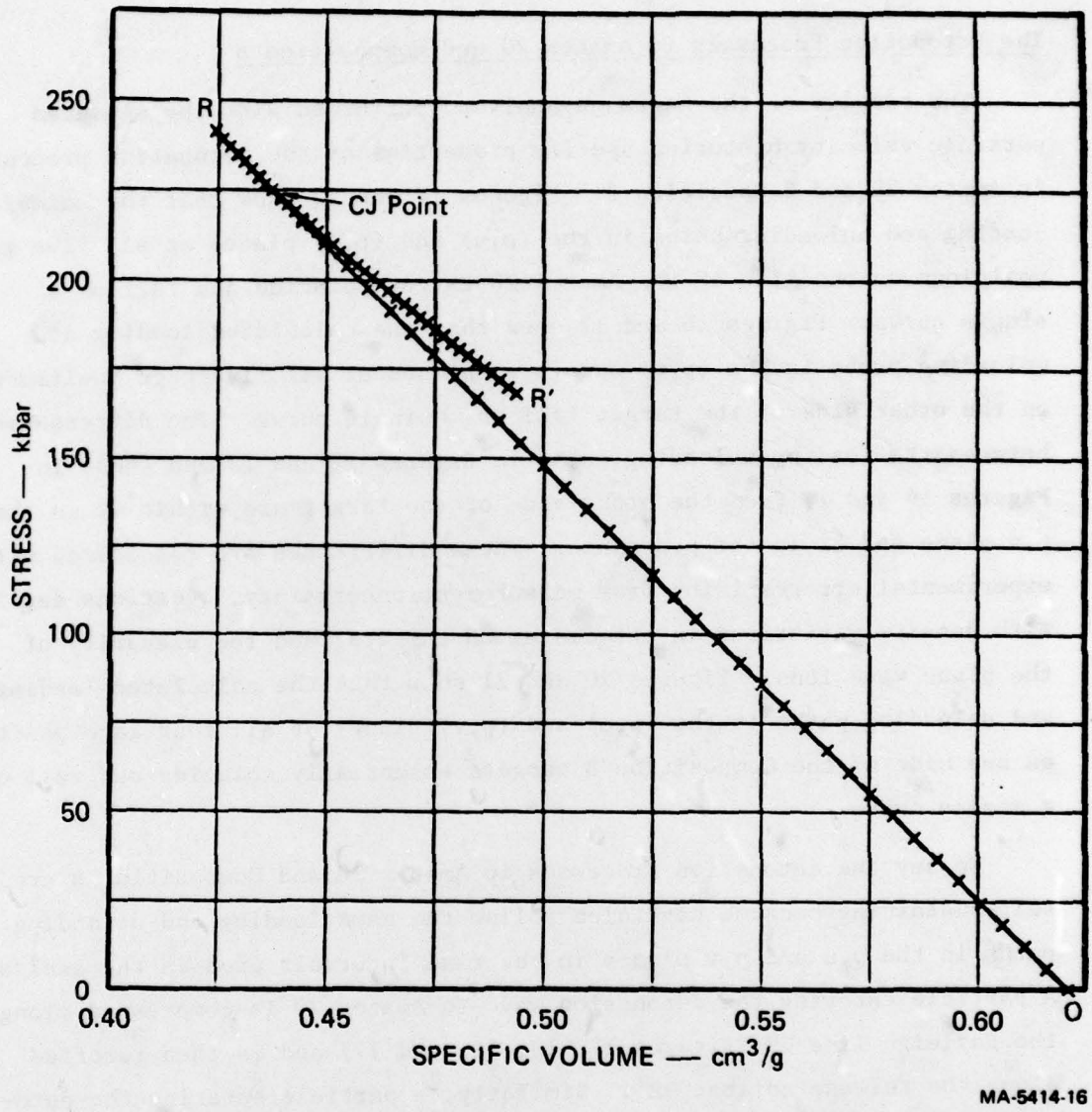

FIGURE 17 LAGRANGE STRESS—SPECIFIC-VOLUME LOAD-UNLOAD PATHS AT THE GAGE POSITIONS IN DETONATING AMATEX 20 CALCULATED FROM THE PARTICLE VELOCITY HISTORIES SHOWN IN FIGURE 14

plots for Composition B generated from the (u,t) records in Figure 9 are shown in Figure 18-21. Figures 10-21 represent the analytical results for the two materials studied in this program; the significance of the labels on states and paths in these figures is discussed later.

The Detonation Processes in Amatex 20 and Composition B

The results of the Lagrange analyses performed with the measured particle velocity histories specify properties of the detonation processes in Amatex 20 and Composition B. Figures 12 and 13 show that the calculated loading and unloading paths in the (p,u) and (p,v) planes at all five gage positions on one side of the Amatex 20 target coincide and fall on a single curve. Figures 16 and 17 show that the calculated loading and unloading paths in the (p,u) and (p,v) planes at all five gage positions on the other side of the target fall on a single curve. The differences between the loading-unloading paths in Figures 12 and 13 and those in Figures 16 and 17 from the other side of the target are within 4% in the p,v plane and 2% in the p,u plane. These differences are considered within experimental error arising from measurement uncertainty, questions dealing with density variations in the Amatex 20 targets, and the planarity of the plane wave lens. Figures 20 and 21 show that the calculated loading and unloading paths in the (p,u) and (p,v) planes at all four gage positions on one side of the Composition B targets essentially coincide and fall on a single curve.

We say the detonation processes in Amatex 20 and Composition B are self-sustaining because particles follow the same loading and unloading paths in the p,u and p,v planes in the time intervals used in the analyses. A particle entering the detonation wave in Amatex 20 is compressed along the Rayleigh line OR (Figures 12, 13, 16, and 17) and is then rarefied along the release adiabat RR'. Similarly, a particle entering the detonation wave in Composition B is compressed along the Rayleigh line OR (Figures 20 and 21), and then rarefied along the release adiabat RR'. Because the loading paths are essentially linear, indicating steady flow, we can calculate detonation velocity from the Rankine-Hugoniot jump condition expressing the balance of momentum, Eq. (2). This was computationally more convenient than reading velocities from time-distance plots.

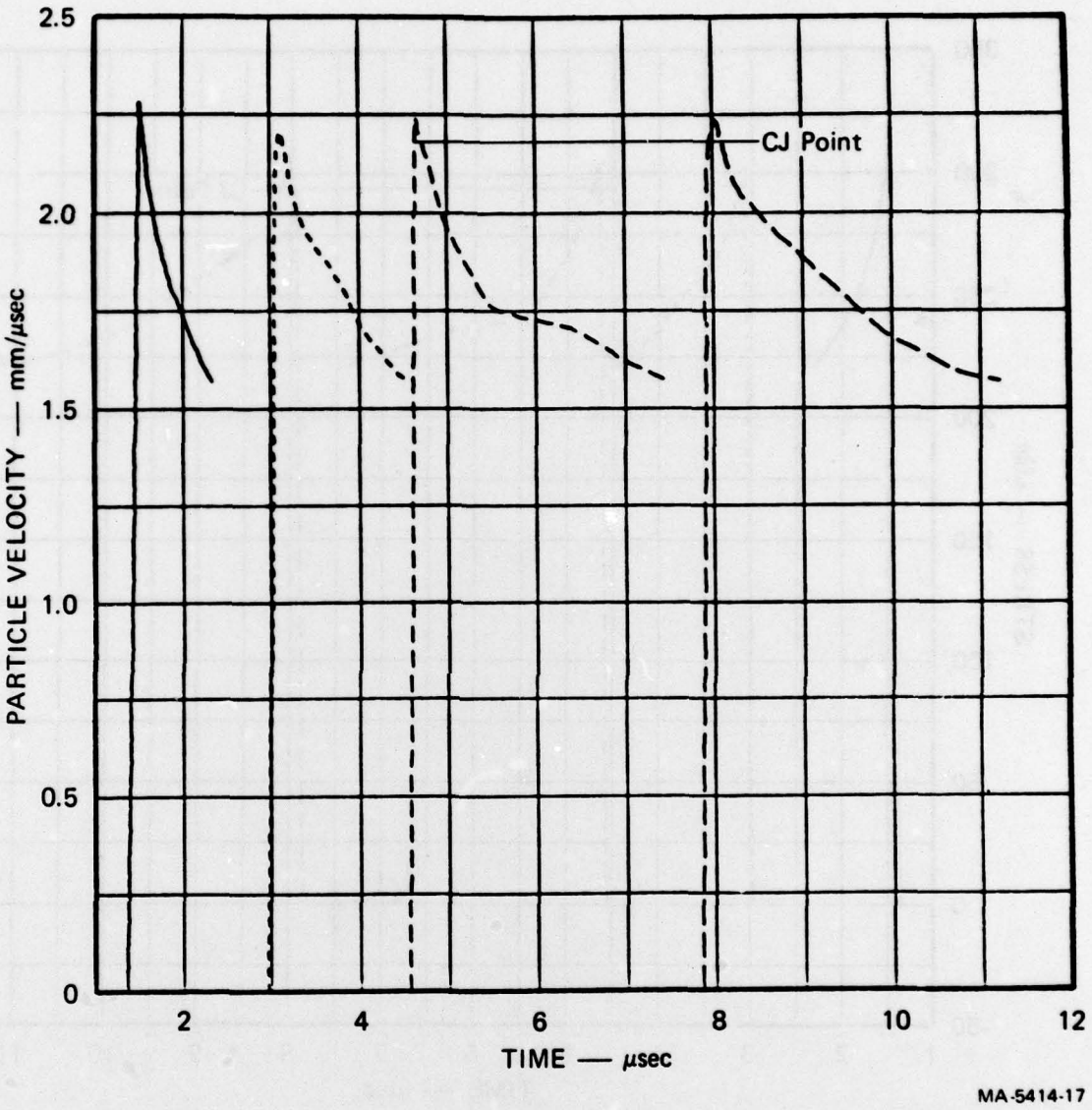

FIGURE 18 SMOOTHED PARTICLE VELOCITY HISTORIES IN DETONATING COMPOSITION B (EXPERIMENT 5, GAGES 6, 8, 9, AND 10) USED IN LAGRANGE ANALYSIS

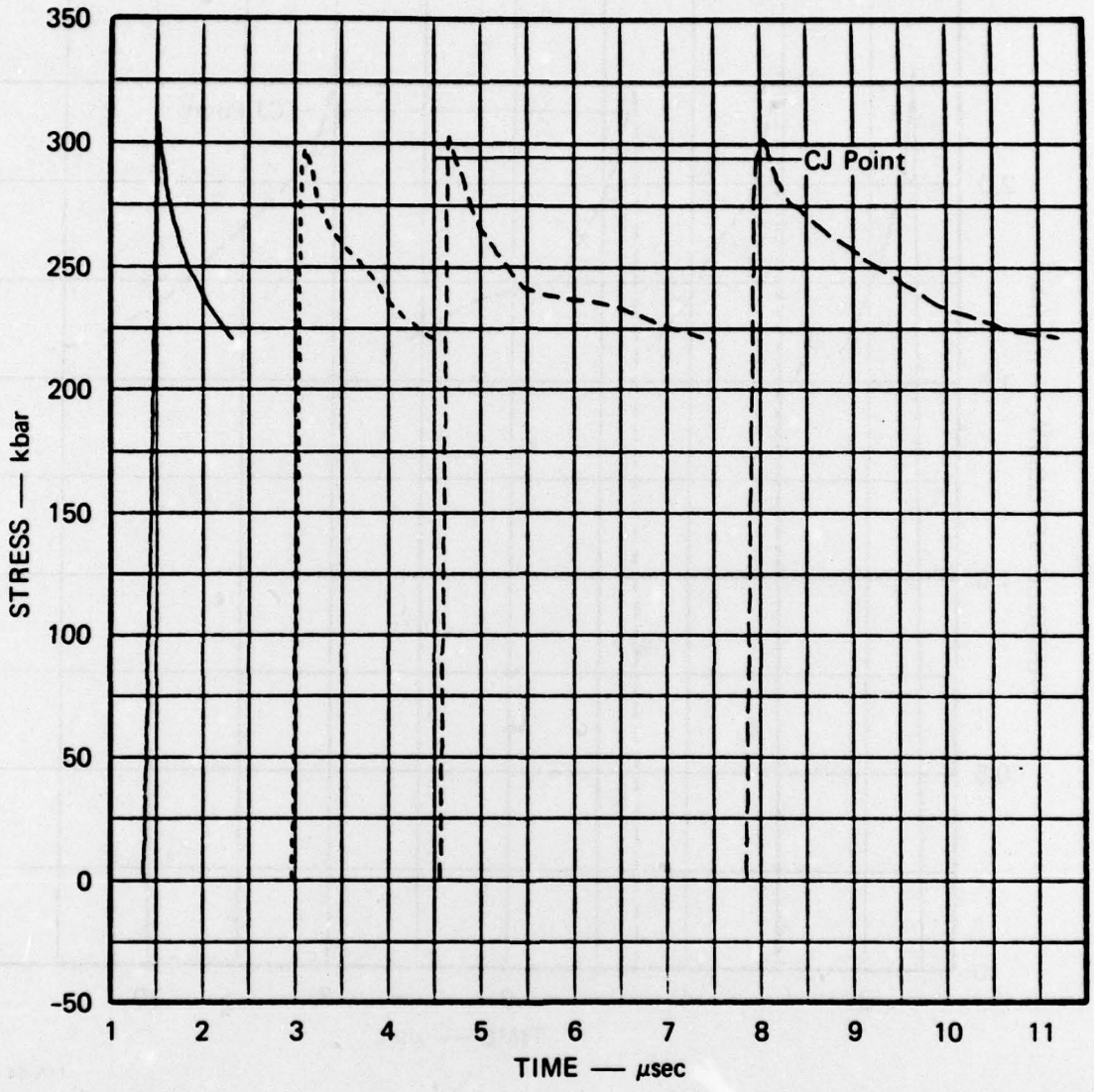

FIGURE 19 LAGRANGE STRESS HISTORIES AT THE GAGE POSITIONS IN DETONATING COMPOSITION B CALCULATED FROM THE PARTICLE VELOCITY HISTORIES SHOWN IN FIGURE 18

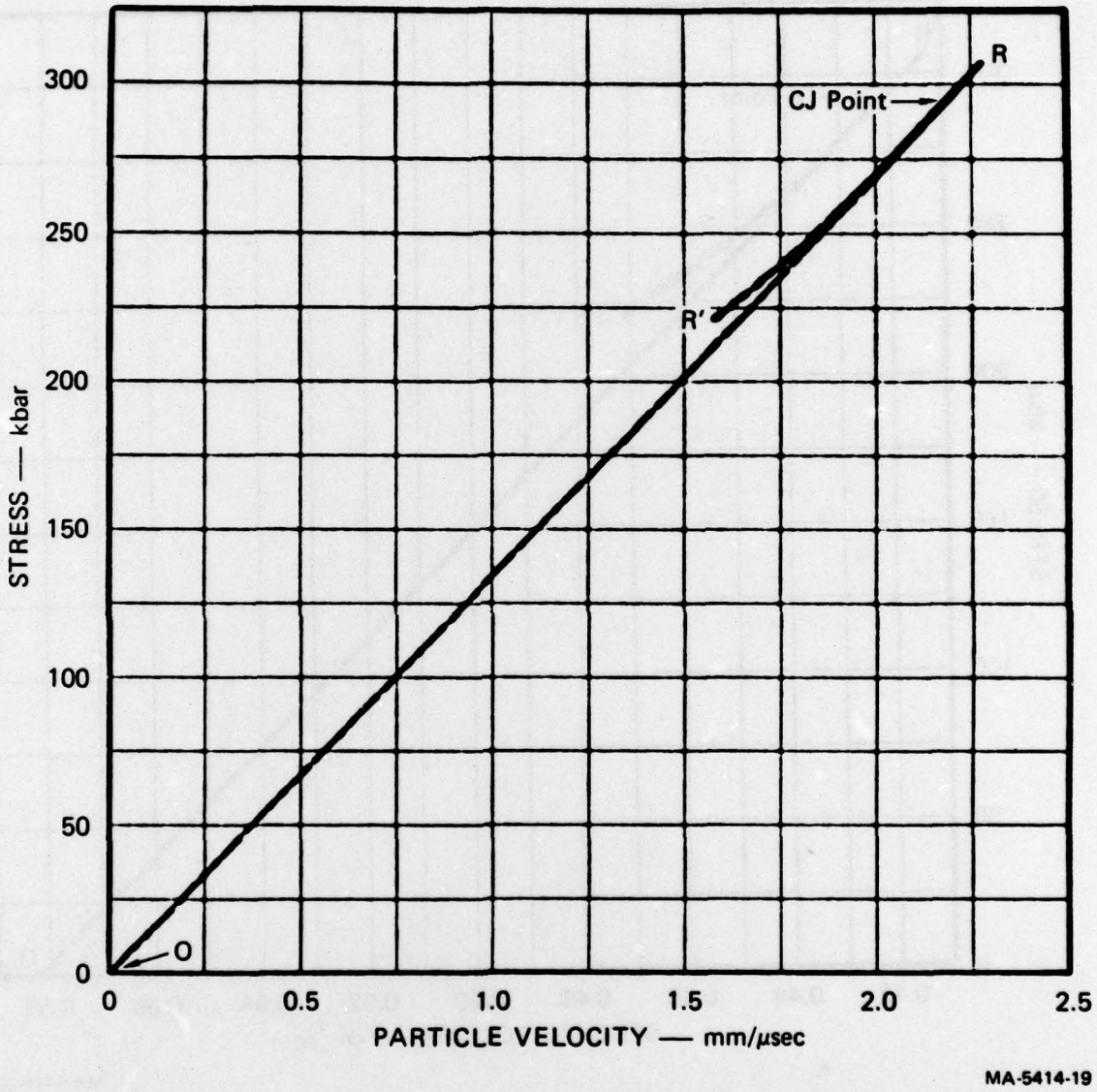

FIGURE 20 LAGRANGE STRESS—PARTICLE-VELOCITY LOAD-UNLOAD PATHS AT THE GAGE POSITIONS IN DETONATING COMPOSITION B CALCULATED FROM THE PARTICLE VELOCITY HISTORIES SHOWN IN FIGURE 18

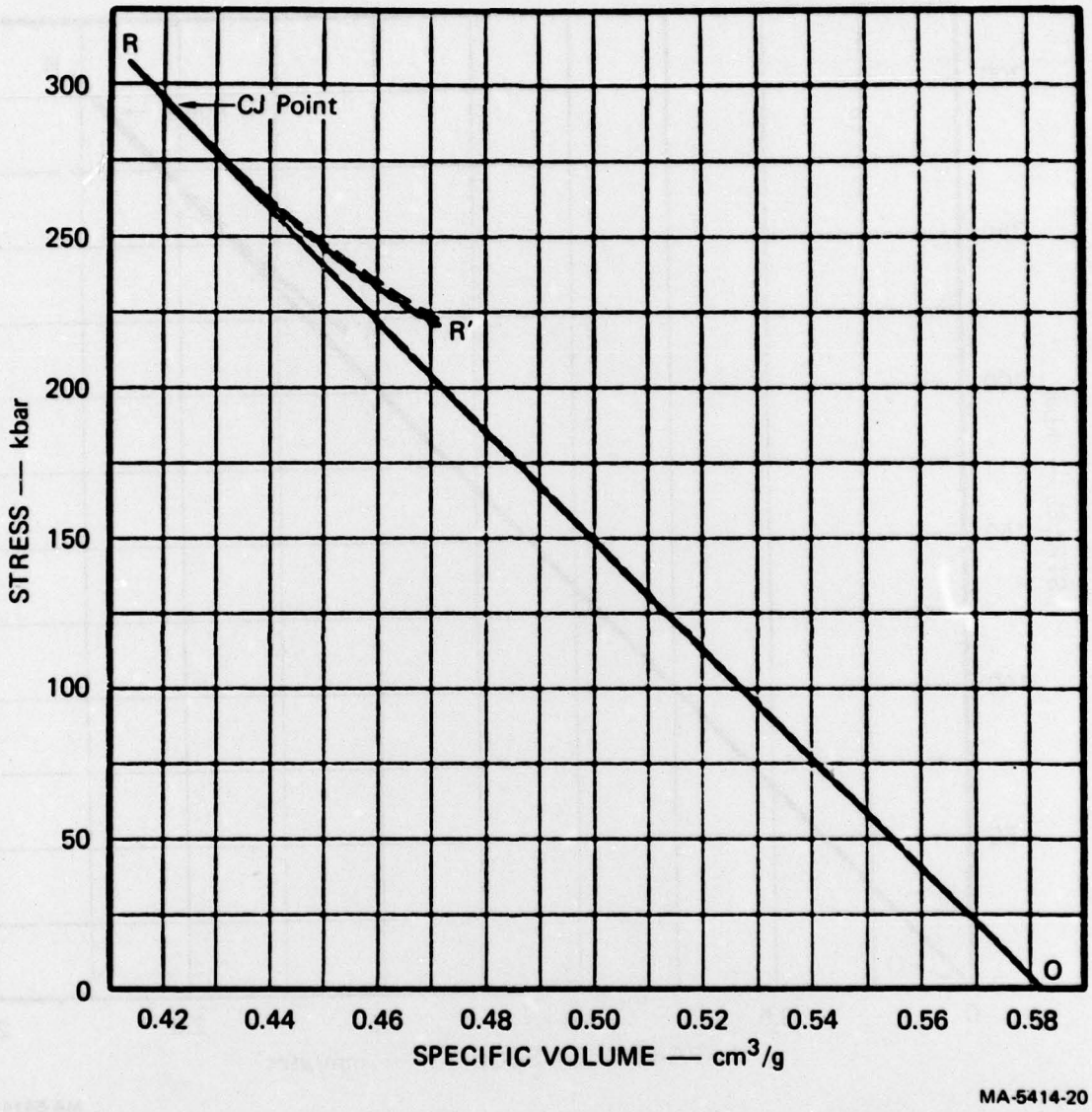

FIGURE 21 LAGRANGE STRESS—SPECIFIC-VOLUME LOAD-UNLOAD PATHS AT THE GAGE POSITIONS IN DETONATING COMPOSITION B CALCULATED FROM THE PARTICLE VELOCITY HISTORIES SHOWN IN FIGURE 18

We applied Eq. (2) between the foot and the peak of the waves by using the measured peak particle velocity and the peak pressure calculated in the Lagrange analysis. In Amatex 20, averaging the data from both sides of the target, the peak particle velocity of 2.18 mm/μs and the peak pressure of 244 kbar give the detonation velocity as 6.95 mm/μs. The peak particle velocity of 2.24 mm/μs in Composition B and the average peak pressure of 302.5 kbar gives the detonation velocity in Composition B as 7.86 mm/μs.

The results of the Lagrange analysis give other properties of the detonation processes in Amatex 20 and Composition B. The calculated loading and loading paths in Figures 12, 13, 16,17, 20, and 21 show that the detonation waves in Amatex 20 and Composition B have a CJ point where the Rayleigh lines OR and the release adiabats RR' are tangent in the (p,u) and (p,v) planes. Because it is difficult to identify the points of tangency from the figures, we use (p,u,v) points calculated in the Lagrange analysis and the CJ condition to determine these CJ points. It is convenient to define the sound speed by the equation $c^2 = kpv$ and express the CJ condition by the equations

$$kpv = (D-u)^2 \tag{43}$$

and

$$k = D/u-1 \ . \tag{44}$$

The CJ points in Amatex 20 and Composition B are identified respectively as the unique (p,v,u) state on each load-release path generated in the Lagrange analysis that simultaneously satisfies Eqs. (43) and (44). Calculations for Amatex 20, using load-unload paths generated from the particle velocity histories shown in Figure 10, give the CJ values P_{CJ} = 225 kbar, u_{CJ} = 2.00 mm/μs, and v_{CJ} = 0.444 cm^3/g, as shown in Figures 12 and 13. The corresponding value of k is 2.51. Examination of the particle velocity and stress histories in Figures 10 and 11 shows that the slopes of these records exhibit a discontinuity at the CJ point. Similar calculations using the Amatex 20 (p,v,u) load-unload paths generated from the particle velocity histories shown in Figure 14 give the CJ values p_{CJ} = 224 kbar, u_{CJ} = 2.02 mm/μs, and v_{CJ} = 0.438 cm^3/g,

as shown in Figures 16 and 17, and a value of k of 2.40. The discontinuities in the slopes of the particle velocity and stress records at the CJ point are apparent in the profiles shown in Figures 14 and 15. The results of these calculations give the average CJ parameters in Amatex 20 as p_{CJ} = 225 kbar, u_{CJ} = 2.01 mm/μs, v_{CJ} = 0.441 cm^3/g, and k = 2.46. Calculations for Composition B using (p,v,u) load-unload paths generated from the particle velocity histories shown in Figure 18 give the CJ values p_{CJ} = 296 kbar, u_{CJ} = 2.19 mm/μs, and v_{CJ} = 0.420 cm^3/g, as shown in Figures 20 and 21. The corresponding value of k is 2.58. In the unloading interval spanned by the Lagrange analysis, the polytropic adiabatic relationship $pv^{2.58} = p_{CJ}\, v_{CJ}^{2.58}$ is a good fit for the release adiabat RR'.

Determination of the CJ point allows estimates of the reaction times in detonating Amatex 20 and Composition B from the particle velocity histories recorded by the gages. The reaction time is defined here as the time it takes a particle entering the wave to reach the identified CJ state. In Amatex 20 the reaction time is 0.3 μs; in Composition B it is 0.1 μs.

5. CONCLUSIONS AND DISCUSSION

Multiple-Lagrange-gage techniques were used to characterize the detonation process in Amatex 20 and Composition B by determining the sequence of states attained along particle paths in these detonating explosives. The states attained during compression and rarefaction in the detonation waves were calculated with the Lagrange analysis from the Lagrange particle velocity histories recorded by the gages in the experiments.

Although exhaustive studies to determine the accuracies of the experimental and analytical methods were beyond the scope of this effort, the results of both appear reasonable, given our present knowledge of the study materials. We know of no abnormal sensitivities or problems associated with the research methods that would cast doubts on the present results and we estimate that they probably can be reproduced to within 10%. We conclude, therefore, that the load-unload paths determined here are meaningful; moreover, we have used them to deduce additional information about the detonation processes in the study materials.

The loading and unloading paths in the pressure and particle-velocity plane and in the pressure and specific-volume plane determined in this work show that the detonation processes are self-sustaining in Amatex 20 and Composition B. Values of the CJ detonation parameters in these explosives were obtained by finding the unique point on the load-unload paths where the calculated values of pressure, specific volume, and particle velocity satisfy the CJ condition. Values of the CJ particle velocities were then used in conjunction with the particle velocity histories to determine the reaction times in Amatex 20 and Composition B.

The fact that the calculated CJ pressures in Amatex 20 and Composition B are lower than their calculated peak pressures leads to the conclusion that the reaction zones in these explosives are partially resolved by present Lagrange gage techniques. It also follows from the particle velocity histories shown in Figures 10 and 18 that the reaction zone in Amatex 20 is longer and therefore more clearly resolved than the reaction zone in Composition B. We seek an explanation for the difference in the reaction times in Amatex 20 and Composition B in terms of the different rates of reaction of RDX, TNT, and NH_4NO_3. Because cast TNT is known to have a much longer reaction time than most conventional high explosives, we postulate that the TNT, and not the RDX, is largely responsible for the experimentally determined reaction time of 0.1 μs in Composition B. We then attribute the longer reaction time of 0.3 μs in Amatex 20 to the slower reacting NH_4NO_3, and take the difference in the reactions times in Composition B and Amatex 20 as evidence that the NH_4NO_3 reacts and supports the propagation of the detonation wave in Amatex 20.

The results of the multiple Lagrange gage study illustrate the limitation of the basic assumption made in the theoretical study. The fact that the reaction zone is partially resolved in Composition B shows that it is unrealistic to treat the front of the detonation wave as a reactive discontinuity. Other properties of the nonideal detonation process derived in the theoretical study can, however, be used to interpret the detonation process in Amatex 20. Because the ammonium nitrate reacts to support a steady-state reaction zone in Amatex 20, the detonation will be ideal if all the ammonium nitrate reacts in the reaction zone, but nonideal if it does not. Thermodynamic calculations are needed to determine how much of the ammonium nitrate reacts in the reaction zone and thereby to determine if the detonation process is ideal or nonideal. Such calculations with the TIGER code are proposed to complete the characterization of the detonation wave in Amatex 20 and to provide a step forward in understanding the role of ammonium nitrate in the detonation process.

The present work is the first application of multiple-Lagrange-gage techniques to the study of the detonation process in condensed explosives. Questions about the precision of the detonation parameters determined in

this work remain unanswered because the accuracy of multiple Lagrange gage techniques for detonating explosives have not been extensively studied. It should be remembered, however, that the detonation parameters are determined in a direct manner from experimental data recorded in detonating explosives. Moreover, these Lagrange techniques provide the only direct method we know for determining detonation parameters. We believe that the present work, probably the most detailed study of Amatex 20 made to date, provides the best information about the detonation process in this explosive.

Calculations to determine the amount of NH_4NO_3 supporting the propagation of the detonation wave in Amatex 20, and multiple-Lagrange-gage studies of other composition containing NH_4NO_3 are proposed to gain an understanding of the role of NH_4NO_3 in the detonation process. Studies to determine the precision and reproducibility of the Lagrange gage techniques are also recommended because they provide the means of quantifying the initiation and detonation processes in condensed explosives.

ACKNOWLEDGMENTS

The authors thank B. Y. Lew for reducing the data of the particle velocity records and for performing the Lagrange analysis.

REFERENCES

1. M. Cowperthwaite and W. H. Zwisler, "TIGER Computer Program Documentation," SRI International Publication No. Z106, Vol. IV.

2. M. Cowperthwaite and J. T. Rosenberg, "Characterization of Initiation and Detonation by Lagrange Gage Technology," SRI International Final Report, ERDA Contract EY-76-C-03-115 Project Agreement 115 (July 1977).

3. A. N. Dremin, K. K. Shvedov, and V. A. Veretennikov, "Research into the Detonation of Ammonite PZhV-20 and Certain Other Explosives," Vzryvnoye delo, 52, No. 9 (1963), UCRL Translation 10405, Nov. 1969.

4. A. N. Dremin and S. A. Koldunov, "Initiation of Detonation by Shock Waves in Cast and Pelletized TNT," Vzryvnoye delo, 63, No. 20 (1967), UCRL Translation 10408, Nov. 1969.

5. D. J. Edwards and J. O. Erkman, "The Measurement of Particle Velocity in Cast TNT," NOLTR 71-19, Naval Ordnance Laboratory, White Oak, Silver Spring, Md., June 1971.

6. D. J. Edwards, J. O. Erkman, and Donna Price, "The Measurement of Particle Velocity in Pressed TNT," NOLTR 72-82, Naval Ordnance Laboratory, White Oak, Silver Spring, Md., Aug. 1972.

7. D. J. Edwards, J. O. Erkman, and Donna Price, "The Measurement of Particle Velocity in Pressed Tetryl," NOLTR 72-83, Naval Ordnance Laboratory, White Oak,Silver Spring, Md., Aug. 1972.

8. S. J. Jacobs and David J. Edwards, "Experimental Study of the Electromagnetic Velocity Gage Technique," Fifth Symposium (International) on Detonation, Pasadena, CA., Aug. 1970, ACR-184, Office of Naval Research, Department of the Navy, Arlington, VA.

9. M. Cowperthwaite and J. T. Rosenberg, "Use of Lagrange Gages to Determine the Energy Release Rate in Condensed Explosives," Draft Final Report prepared for U.S. Army Ballistic Research Laboratory, Contract DAAD05-74-C-0756, SRI International, Menlo Park, CA., 94025, July 1979.

10. J. R. Reitz and F. J. Milford, Foundations of Electromagnetic Theory, Addison-Wesley Publishing Company, 1960.

11. Lynn Seaman, "Lagrangian Analysis for Multiple Stress or Velocity Gages in Attenuating Waves," J. Appl. Phys. 45, 4303, 1974.